SANDIA REPORT
SAND2020-10403
Printed Click to enter a date

Sandia National Laboratories

Experimental and Theoretical Studies of Ultrafast Vibrational Energy Transfer Dynamics in Energetic Materials

Krupa Ramasesha, Mitchell Wood, Neil C. Cole-Filipiak, Robert Knepper

Prepared by
Sandia National Laboratories
Albuquerque, New Mexico
87185 and Livermore,
California 94550

Issued by Sandia National Laboratories, operated for the United States Department of Energy by National Technology & Engineering Solutions of Sandia, LLC.

Available to DOE and DOE contractors from
U.S. Department of Energy
Office of Scientific and Technical Information
P.O. Box 62
Oak Ridge, TN 37831

Telephone: (865) 576-8401
Facsimile: (865) 576-5728
E-Mail: reports@osti.gov
Online ordering: http://www.osti.gov/scitech

Available to the public from
U.S. Department of Commerce
National Technical Information Service
5301 Shawnee Rd
Alexandria, VA 22312

Telephone: (800) 553-6847
Facsimile: (703) 605-6900
E-Mail: orders@ntis.gov
Online order: https://classic.ntis.gov/help/order-methods/

ABSTRACT

Energy transfer through anharmonically-coupled vibrations influences the earliest chemical steps in shockwave-induced detonation in energetic materials. A mechanistic description of vibrational energy transfer is therefore necessary to develop predictive models of energetic material behavior. We performed transient broadband infrared spectroscopy on hundreds of femtoseconds to hundreds of picosecond timescales as well as density functional theory and molecular dynamics simulations to investigate the evolution of vibrational energy distribution in thin film samples of pentaerythritol tetranitrate (PETN), 1,3,5-trinitroperhydro-1,3,5-triazine (RDX), and 2,4,6-triamino–1,3,5-trinitrobenzene (TATB). Experimental results show dynamics on multiple timescales, providing strong evidence for coupled vibrations in these systems, as well as material-dependent evolution on tens to hundreds of picosecond timescales. Theoretical results also reveal pathways and distinct timescales for energy transfer through coupled vibrations in the three investigated materials, providing further insight into the mechanistic underpinnings of energy transfer dynamics in energetic material sensitivity.

ACKNOWLEDGEMENTS

The authors thank Robert Harmon for programming the data acquisition software, Michael Marquez for depositing the PETN, TATB and RDX samples, Paul Schrader for assistance with laboratory set-up, and Deneille Wiese-Smith for handling storage and transport of the energetics. The authors are grateful to Leanna Minier and Darcie Farrow for their useful insights and thank Jeffrey Kay for his critical involvement at the outset of this project.

CONTENTS

LIST OF FIGURES

This page left blank

ACRONYMS AND DEFINITIONS

Abbreviation	Definition
VET	Vibrational Energy Transfer
PETN	Pentaerythritol Tetranitrate
TATB	2,4,6-triamino–1,3,5-trinitrobenzene
RDX	1,3,5-Trinitroperhydro-1,3,5-triazine
FOV	Field of View
SEM	Scanning Electron Microscopy
DFT	Density Functional Theory
MD	Molecular Dynamics
DoS	Density of States
2PhDoS	Two-Phonon Density of States
MP	Müller-Plathe
GLE	Generalized Langevin Equations
OPA	Optical Parametric Amplifier
DFM	Difference Frequency Mixing
fs	Femtoseconds (1 fs = 10^{-15} s)
ps	Picoseconds (1 ps = 10^{-12} s)
IR	Infrared
BBIR	Broadband Infrared
FT	Fourier Transform
IAP	Interatomic Potential

1. INTRODUCTION

Complex energy transfer processes underpin the conversion of mechanical energy to chemical energy during shockwave-induced detonation in energetic materials. The cascade of processes contributing to this shock-to-detonation transition spans several decades in time, ranging from vibrational motion that occur on femtosecond timescales to chemical reactions that occur on microsecond or longer timescales. While a significant body of work exists on this topic,[1-4] much is unknown about the mechanism of shock-induced reaction initiation and the influence of properties – such as chemical structure, crystalline morphology or defects – on the sensitivity of energetic response to shock. The work presented here tests aspects of one hypothesized mechanism for energetic initiation – the phonon up-pumping mechanism[5-6] – and investigates the influence of chemical structure on the observed femtosecond to picosecond vibrational energy transfer (VET) dynamics.

The phonon up-pumping mechanism hypothesizes that the large anharmonicities of phonon modes excited behind a shockwave results in uphill vibrational energy transfer to select molecular vibrations, ultimately resulting in bond dissociation and reaction.[5-6] Vibrational up-pumping and vibrational cooling work in tandem, as energy is shuffled between different molecular and lattice modes in the material.[7] There have been many studies of VET in energetic material analogs and solvated energetics using ultrafast Raman and IR spectroscopy (for examples, see Refs. 8-11). However, VET is strongly dependent on the phase of matter and the environment, requiring that these measurements be performed on neat energetic solids to obtain a better understanding of energy transfer in these systems.[12-14] Prior to our work, there were two studies of VET in neat energetic solids, where ultrafast two-dimensional infrared spectroscopy[14] and ultrafast coherent anti-Stokes Raman spectroscopy[15] were used to understand vibrational coupling and energy transfer in PETN and RDX, respectively. Much insight was gained from these measurements on the influence of hydrogen bonding, vibrational coupling, and the extent of vibrational delocalization on the femtosecond to picosecond vibrational dynamics. The infrared experiments,[14] however, were limited by the narrow bandwidth of the infrared pulses used, allowing only single bands of vibrations to be probed, thus precluding a global view of VET. The ultrafast Raman studies of RDX used broadband excitation below 1000 cm^{-1} to understand vibrational coupling, but this study was confined to low frequency vibrations.[15] Given the myriad infrared transitions present in energetic materials and the critical role they play in channeling energy to the reaction coordinates responsible for initiation, a broadband view of VET across all vibrational modes is necessary.

In order to establish timescales and pathways for VET, we performed ultrafast broadband infrared spectroscopy, density functional theory (DFT) and molecular dynamics (MD) simulations on thin films of three energetic materials: pentaerythritol tetranitrate (PETN), 1,3,5-trinitroperhydro-1,3,5-triazine (RDX), and 2,4,6-triamino–1,3,5-trinitrobenzene (TATB). Broadband pulses generated from a laser-driven plasma-based source allowed probing of all infrared-active vibrations in the mid-IR region.[16] The three energetic materials were chosen due to their differing shock sensitivities, with TATB being highly insensitive to shock, and PETN being the most shock sensitive of the three materials.[17] Experimentally, our method for studying VET in these materials utilized a narrowband infrared "pump" pulse to excite specific infrared bands in the system and a broadband infrared "probe" pulse to monitor the evolution of all infrared-active modes in the mid-infrared region on hundreds of femtoseconds to hundreds of picosecond timescales. Computational work utilizing DFT involved mapping the harmonic and anharmonic terms of the potential energy surface in order to identify scattering pathways for VET. In addition to these static calculations, MD simulations characterized the relaxation times of pumped vibrations as well as vibrations coupled via VET pathways.

2. METHODS

2.1. Experimental

The apparatus used for ultrafast broadband infrared spectroscopy is described in detail in Refs. 18-19. Briefly, the ~50 fs, 780 nm output from a commercial Ti:Sapphire laser is split into two arms. One arm is sent into an optical parametric amplifier (OPA), whose signal and idler outputs are difference frequency mixed (DFM) and sent through a narrow bandpass filter to generate micro-Joule level, tunable, narrowband (~200 cm^{-1} full-width-at-half-maximum bandwidth) mid-infrared pulses that serve as pump pulses to excite specific infrared transitions in the material. The other arm of the laser output is first frequency-doubled, the fundamental and doubled light are then polarization-matched and temporally overlapped, and finally sent onto a 50 mm dielectric coated concave mirror. The concave mirror focuses the beams in flowing nitrogen gas at ambient pressure to generate a plasma. The plasma radiates light that spans visible to the terahertz frequencies; we select the mid-infrared portion by passing the plasma emission through a 0.5 mm thick Si wafer.[16, 20] These weaker broadband infrared (BBIR) pulses serve as the probe to monitor all IR-active vibrations within the detected bandwidth of 800 – 4000 cm^{-1}. The pump and probe pulses are delayed with respect to each other using a motorized optical delay line, then focused and overlapped in the sample, and the transmitted probe pulse is sent into an infrared spectrometer and detected on a 64-element liquid nitrogen cooled HgCdTe array detector. The $1/e^2$ focal diameters of the pump and probe beams at the sample position are 310 μm and 220 μm, respectively. Experiments involving narrowband IR pump and broadband IR probe were performed with parallel relative polarizations of the pump and probe.

For transient infrared spectra where pump and probe frequencies are the same, the output from the OPA-DFM set-up is split into a ~5%/95% ratio, where the 5% arm serves as the probe and the 95% arm serves as the pump. In order to minimize scatter of the pump beam at the sample from reaching the detector, these degenerate pump-probe experiments are performed with the pump polarization perpendicular to the probe polarization.

Pump-probe experiments in PETN used three different pump frequencies in order to excite different infrared bands in the material. The first experiment used a narrowband pump pulse centered at 1661 cm^{-1}, with ~200 cm^{-1} of bandwidth and 2 μJ pulse energy; this work is published in Ref. 18 and will not be detailed in the present report. The second experiment used narrowband pump pulses centered at 1256 cm^{-1} with 1.6 μJ pulse energy. The pump-probe cross-correlation widths for the above pump frequencies measured using the technique described in Ref. 18-19, was ~200 fs, indicating the instrument response and the shortest time delay we can resolve. The third experiment used the narrowband pump pulse centered at 1060 cm^{-1} with 1.2 μJ pulse energy. The pump-probe cross-correlation width with 1060 cm^{-1} pump pulses was ~300 fs.

Experiments in TATB used pump pulses with center frequencies at 1533 cm^{-1} and at 1190 cm^{-1} with pulse energies of 1.6-1.8 μJ and 1.4 μJ, respectively. Experiments in RDX used pump pulses centered at 1533 cm^{-1} with pulse energy of 2.2-3 μJ. The pump-probe cross-correlation width with 1533 cm^{-1} and 1190 cm^{-1} pump pulses was ~200 fs.

2.2. Theoretical

The main goal of the theory and computational side of this project is to provide an alternate means from the experiments to study VET, where we can both test experimental observations further and provide predictions to narrow the number of necessary experiments. As is the case with all computational work, we need to be aware of where approximations are being made and how this impacts our ability to do one-to-one comparisons between experiment and simulation. The following sections will discuss the methods employed, the data that are generated, but most importantly the approximations that are made within these methods.

2.2.1. Density Functional Theory

To begin, DFT is considered a first-principles (*ab initio*) computational method, in that it makes the least restrictive approximations of the true physics of the system. At its core, DFT circumvents solving for all of the quantum mechanical wavefunctions via the Schrödinger Equation by instead solving for the density of electrons within a given volume of material.[21-22] This is further simplified to just be the density of valence electrons given that most core-electron states play a very minimal role in material properties near ambient conditions. It is reasonable to assume this additional approximation, *i.e.* the use of a pseudopotential for core electron states, will not affect our comparison to experiments where mid-IR pulses will predominately excite v = 0→1 vibrational states far below the energetic transitions attributed to core electrons. Limiting DFT calculations to valence electrons also saves a tremendous amount of compute time as the time to solution scales cubically with the number of electrons treated in the self-consistent field operation.

For the present work, accuracy of the DFT calculation is determined by the convergence of the iterative solver with respect to the predicted forces on each atom. Comprehensive reviews on the subject of DFT accuracy[23] focus on choices in the kinetic energy cutoff of the plane wave basis set and the reciprocal lattice sampling density (k-point grid). These choices depend on which material system is of interest, and as such will be defined per-material in the following results section.

The DFT work here is not focused on the light absorption process and immediate electron-phonon coupling events that precede VET. Rather, we aim to use DFT to map VET cascades through phonon-phonon interactions. Herein we use "phonon" and "vibration" interchangeably when discussing the molecular crystals of interest as molecular crystals demonstrate both low frequency crystal deformations (usually called phonons) as well as high frequency intra- and inter-molecular modes (usually called vibrations) with a continuous spectrum of modes between them. In doing so, we can leverage much of the language used and background work in both solid-state physics (thermal transport theory) and physical chemistry (infrared spectroscopy).

In order to predict the steady-state thermal conductivity of solids, many researchers rely on the relaxation time approximation in order to solve the Boltzmann transport equation. From first-principles calculations, this approximation requires either an assumption of the per-mode linewidths or direct calculation based on phonon-phonon scattering. The end goal of our calculations is not a prediction of the thermal conductivity, but rather the change in scattering intensities subject to some frequency-localized excitation of the system.

In order to predict two phonon scattering events (into a third phonon), the first anharmonic moment of the potential energy surface is required[24-26]. Consider a model Hamiltonian with a moment expansion of the potential energy as follows:

$$H = \frac{1}{2}\sum_{i,\alpha} m_i {v_\alpha}^2 + \sum_i^N P_i \qquad (1)$$

$$P_2 = \frac{1}{2}\sum_{i,\alpha}\sum_{j,\beta}\phi_{\alpha\beta}u_{\alpha,i}u_{\beta,j} = \sum_{\lambda}\hbar\omega_{\lambda}\left(\frac{1}{2} + \hat{a}_{\lambda}^{\dagger}\hat{a}_{\lambda}\right) \quad (2)$$

where $u_{\alpha,i}$ and $u_{\beta,j}$ are the displacements of (i,j) atoms in the direction of the vibrational mode (α,β) and the force constant of this oscillator is $\phi_{\alpha\beta}$. Written another way, the right hand side of equation 2 shows the creation/annihilation operator analog for vibrational modes λ of frequency ω. Force constants of all moments in the expansion can be extracted from DFT (or MD for that matter) through finite differences of forces, as described in Equation 3.

$$\phi_{\alpha\beta}(i,j) = \frac{\partial F_{\beta}(j)}{\partial r_{\alpha}(i)} = \frac{F_{\beta}(j;\Delta r_{\alpha}(i)) - F_{\beta}(j)}{\Delta r_{\alpha}(i)} \quad (3)$$

Note that higher order force constants involve displacements of multiple atoms and it becomes quite cumbersome to enumerate and calculate all possible combinations, though some of these force constants are equivalent based on the symmetry of the crystal. The collection of force constants are then used to construct the dynamical matrix (tensor) which establishes an eigenvalue problem for the first harmonic (anharmonic) representation of the vibrations. Automation of the collection and curation of these force constants is achieved through the open source software, Phonopy.[26] Calculation of the force constants themselves is carried out through the plane wave basis DFT code VASP for all materials of interest.[21-22] As mentioned previously the primary quantity of interest are the linewidths; where scattering cross-sections are neglected this is equivalently the inverse of the two-phonon density of states (2PhDoS). The 2PhDoS quantifies how many different scattering events are possible into a given frequency, subject to conservation of energy and scattering within the Brillion Zone.

$$J^{+}(q,\omega) = \frac{1}{N}\sum_{\lambda',\lambda''}\Delta(-q+q'+q'')(n_{\lambda'} - n_{\lambda''})[\delta(\omega + \omega_{\lambda'} - \omega_{\lambda''}) - \delta(\omega - \omega_{\lambda'} + \omega_{\lambda''})] \quad (4)$$

In Equation 4, $\Delta(-q+q'+q'') = 1$ when $(-q+q'+q'')$ is a reciprocal lattice vector and zero otherwise, Dirac deltas enforce energy conservation and n_{λ} are the Bose-Einstein populations for modes λ' and λ''. A summation over reciprocal lattice vectors is computed on a 5 × 5 × 5 sampling mesh of the Brillion Zone, leaving the 2PhDoS only as a function of frequency ($J(\omega)$). To approximate the excitation caused by the mid-IR pump, the Bose-Einstein populations are perturbed by adding a Gaussian of width 66 cm^{-1} at the pump frequency. In order to isolate the scattering events that are affected by the population perturbation, we look at the difference between a pair of 2PhDoS with and without the perturbation, *i.e.* Δ2PhDoS. Importantly, in the analysis of the 2PhDoS is that scattering events will be predicted where no native vibration (one-phonon DoS) exists in the material, which requires extra scrutiny when comparing results directly to experiments.

Infrared spectra can be calculated from the harmonic expansion of the potential energy and Born effective charges of these vibrations can be calculated from Density Functional Perturbation Theory, we use the implementation native to VASP.[27-28] The intersection of the Δ2PhDoS and predicted IR spectra will form the main comparison between DFT and pump-probe experiments; these are vibrations that are coupled to the perturbation and are IR-active (observable by the probe pulse).

2.2.2. Molecular Dynamics Simulations

The next simulation method that was utilized in this work is classical Molecular Dynamics (MD), where the focus was on the dynamic process of VET within a material. As a particle-based computational tool, MD has broad applicability since particles can be made to represent atoms,

molecules or even macroscopic objects like glaciers, continents and planets. The connecting feature throughout these applications is time-integration of particle trajectories via Newton's equations of motion, which implies inter-particle forces are calculated at each time step. For the present study, these forces could be taken directly from DFT, but this would severely limit the accessible timescale. Alternatively, calculation of local forces around atoms offers a much greater computational efficiency that allows for orders of magnitude larger simulations that scale linearly with the number of atoms. The interatomic potential (IAP) that captures these local forces on atoms is the leading approximation made in all MD simulations, and special care is needed to construct and validate an IAP. It is worth noting that for all IAP these are classical, not quantum, dynamic simulations, and there is no notion of quantized vibrational excitations. For each of the energetic materials studied here, we use a non-reactive IAP that approximates the true many body forces as an expansion of two-, three- and four-body bonded interactions as well as pair-wise, long-range electrostatics and dispersion interactions. Each of the IAP for PETN,[29] RDX,[30] and TATB[31] are implemented in the Sandia-developed LAMMPS MD software package, which is used throughout this work.[32]

As an alternative to the perturbative potential energy expansion approach used with DFT, characterization of the vibrational spectrum within MD can be collected through a Fourier transform (FT) of atomic velocities.[33] In order to resolve the full (0–3500 cm^{-1}) vibrational spectral range, the sampling frequency to output atom velocities needs to be quite small ($\Delta t = 5$ fs) and the total sampled trajectory at least ~10 ps. The FT of this kinetic energy spectrum yields the power spectrum of vibrations ($P(\omega)$, see equation 5); a normalization by the total kinetic energy results in the total vibrational density of states, which includes both IR active and inactive modes. Calculation of the IR spectrum is taken from MD as the FT of the first time derivative of the dipole moment, following our previous work.[34] The main challenge with this MD analysis is resolving spectral changes on timescales relevant to VET, which are sub-picosecond to picoseconds. Following our previous work,[33] we can manipulate trajectory segments from many independent, but statistically equivalent simulations in order to achieve spectrally well resolved DoS at ~1 ps intervals. Presently, a 2D-DoS from MD is assembled from forty independent simulation trajectories, each of 1.28 ps in length and a sampling interval of 5 fs. In house analysis tools are used to compute the fast FT of each of these trajectories, code available upon request.

$$P(\omega) = \frac{\beta\tau}{N}\sum_{j=1}^{3N} m_j \left|\sum_{n=0}^{N-1} v_j(n\Delta t)e^{-2\pi i\omega n\Delta t}\right|^2 \qquad (5)$$

Thermostats, as they are colloquially known, in MD are an important part of all MD simulations because they dictate which thermodynamic ensemble you are sampling your trajectory from. For example, a lack of any thermostat has conserved quantities of number of particles (N), volume of the cell (V) and total energy of the system (E). This NVE simulation is decoupled from any external stimulus and thus is equivalent to the micro-canonical ensemble. Where a thermostat is utilized, the temperature, rather than total energy, is a conserved quantity and there are many variations of how to implement velocity re-scaling in order to mimic the infinite thermal bath coupled to the simulation.[35-39] Langevin thermostats add a Gaussian random noise term to the velocity of all atoms that is scaled proportional to the temperature of the bath. In most simulations, the Gaussian random noise term has no time correlation, meaning that there is no preferential coupling of the bath to a subset of vibrations. However, this preferential coupling, termed a "colored thermostat", is precisely what is needed for our MD simulations to match the pump-probe experiments detailed elsewhere in this report.

The theory behind the Generalized Langevin Equations (GLE) is detailed in works by Ceriotti[40-41] and work by Dettori[42], which show how the method can be used for pump-probe

simulations. The goal here is to adjust the thermostat perturbations such that a preferential resonance between molecular vibrations and the thermal bath is established. To ensure that the target mode is held at a higher temperature than the remaining vibrations in the material, we extend the "pump" duration for much longer times than what is used in experiments. The set of simulations – run for each material and target vibration – each establish the non-equilibrium vibrational excitation over a 10 ps period, after which the excitation is removed and the simulation is left to evolve in the micro-canonical ensemble for an additional 100 ps with trajectory segments gathered every 1.28 ps. This process is repeated forty times for each target mode in order to accumulate enough trajectory segments at each time interval to calculate well resolved spectra. Infrared active vibrations are chosen as target modes for direct comparison to experiments. Comparing each time segment of the vibrational spectra of a GLE pumped system to an equilibrium (equipartition of kinetic energy among vibrations) spectra allows us to identify when the system has fully relaxed and thus fit relaxation time constants to individual modes.

2.3. Sample Preparation

Thin films of the explosives PETN, RDX, and TATB were vapor-deposited in a custom-designed high-vacuum system onto 1-mm-thick, 25-mm-diameter substrates of both CaF_2 and BK-7 glass. Deposition was performed at a typical base pressure of 1×10^{-6} Torr. Films were deposited using an effusion cell thermal deposition source to a nominal thickness of 2 – 3 μm. Films on CaF_2 substrates were used for the experiments described above, while those on BK-7 substrates were used for microstructure characterization.

Microstructure characterization was performed using scanning electron microscopy (SEM) to image the top surface and a fracture cross-section of films of each material. Samples were coated with ~5 nm of iridium prior to imaging to mitigate surface charging. Images were collected using a Zeiss GeminiSEM 300 operating with a 1.1 kV accelerating voltage and using the secondary electron detector.

Representative SEM images of the TATB and RDX samples are shown below in Figure 2-1; note the different fields of view (FOV) for each image. Images and descriptions of the PETN microstructure can be found elsewhere.[18] The films all display a columnar morphology, with columns oriented perpendicular to the substrate. The TATB films have a lateral grain size of ~200 nm. Numerous protrusions consisting of one or two grains stick out from the surface to a height of up to 100 nm. In the RDX films, small hillocks with lateral sizes ranging from a few μm up to ~10 μm appear to rise about 100 – 200 nm above the background. In contrast to the protrusions in the TATB films, these hillocks are composed of many grains with lateral grain sizes of ~0.5 – 1 μm.

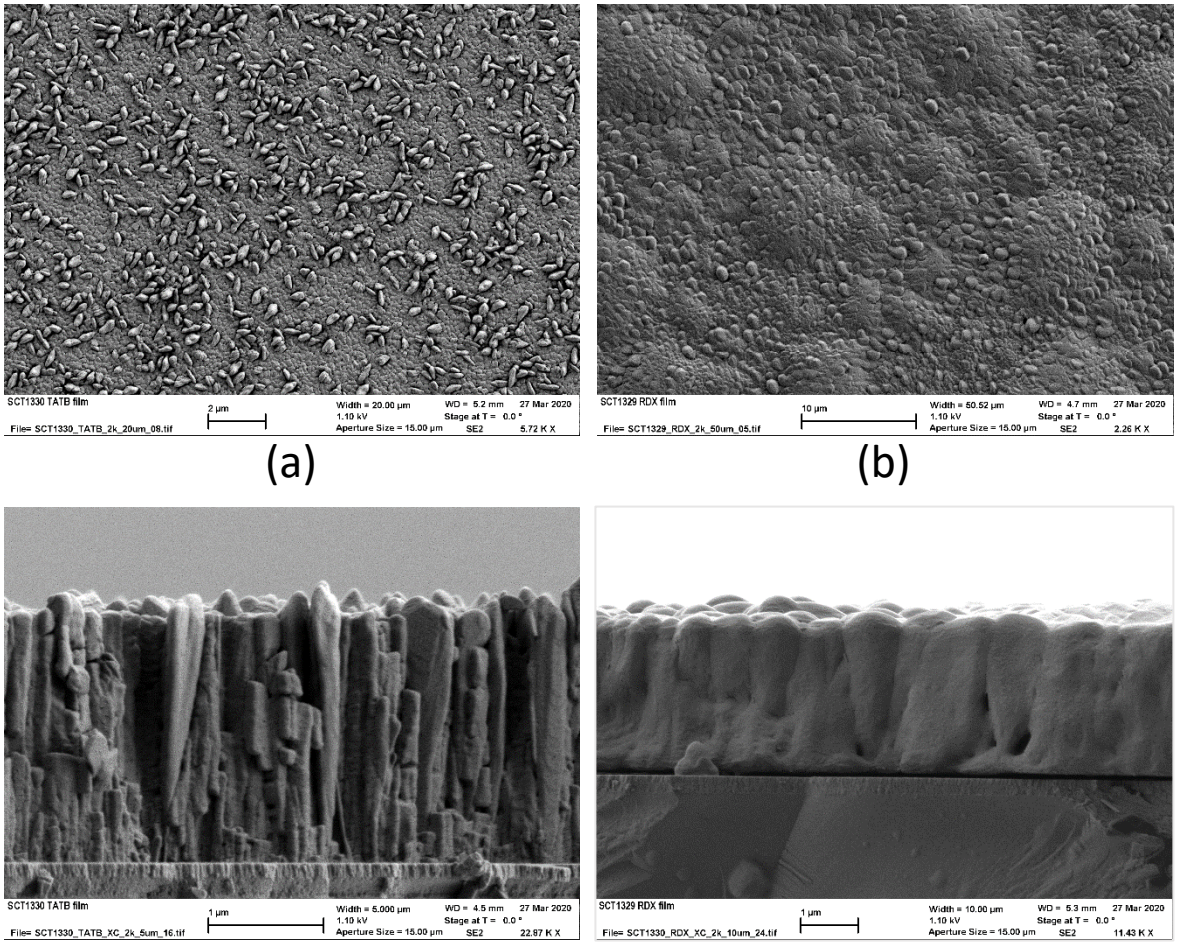

Figure 2-1. SEM images of the top surface and fracture cross-section of vapor-deposited TATB and RDX films. (a) Top surface of TATB (20 µm FOV); (b) Top surface of RDX (50 µm FOV); (c) Cross-section of TATB (5 µm FOV); and (d) Cross-section of RDX (10 µm FOV).

3. RESULTS AND DISCUSSION

3.1. Pentaerythritol Tetranitrate (PETN)

3.1.1. Femtosecond Infrared Spectroscopy Results

Below 1700 cm^{-1}, PETN displays eight infrared absorption bands, and we perform mode assignments of these bands based on our DFT calculations and Ref. 43 (see Ref. 18 for the PETN infrared spectrum and detailed mode assignments from DFT). The vibrational band at 1660 cm^{-1} is primarily the NO_2 asymmetric stretching vibration, with some mixing with the overtone vibrations of the broad nitrate ester ($RO-NO_2$) stretching modes near 860 cm^{-1} through a Fermi resonance. The remaining modes near 1480, 1390, 1280, 1040, 1000, and 940 cm^{-1} comprise the alkyl skeletal vibrations (CH_2 scissoring, C–C–C deformation, etc.), with NO_2 symmetric stretch character contributing to the mode at 1280 cm^{-1}.

VET dynamics following excitation of the 1660 cm^{-1} mode has been published in Ref. 18; we direct the reader to the results, analysis and interpretation presented therein as a point of comparison with the results presented in this report. Here, we follow our previous study[18] with an investigation of VET following excitation at 1256 cm^{-1} as well as at 1060 cm^{-1}. Figure 3-1 and 3-2 display false color maps of the temporal and spectral behavior of transient infrared signal of PETN following 1256 cm^{-1} and 1060 cm^{-1} excitations, respectively. For isolated vibrational modes, transient infrared spectra at the earliest time delays (subsequent to a $v=0\rightarrow1$ pump-induced excitation of an infrared transition) appear as positive-negative doublets. The positive absorption (shown as red regions in all of the false color maps in this report) corresponds to probe-induced absorption from the $v=1$ to higher lying vibrational states, and the negative absorption (or bleach, shown as blue regions in all the false color maps herein) is due to probe-induced stimulated emission of vibrationally excited population back to the $v=0$ state. At long time delays, thermal or non-thermal changes to the population in low frequency phonon modes modify the probed high frequency vibrations, resulting in contributions to the transient signal from a shifted $v=0\rightarrow1$ transition, a transient absorption or bleach from a long-lived vibrationally excited state, or both.

The pump pulse centered at 1256 cm^{-1} excites the vibrational band at 1280 cm^{-1} that is characterized by the NO_2 symmetric stretch vibration and alkyl skeletal modes. The vibrational dynamics observed in this experiment closely mirror the dynamics observed following excitation of the 1660 cm^{-1} mode. The appearance of bleach features at all IR-active vibrations within the instrument time resolution of 200 fs supports the fact that PETN consists of strongly coupled vibrations. Following the sub-picosecond response, the σ(1 ps) to σ(10 ps) dynamics is observed as a vibrational cascade at the high frequency vibrations. The σ(100 ps) evolution is evident for modes below 1000 cm^{-1} that correspond to the nitrate ester stretching vibration and alkyl skeletal modes, either due to VET occurring from long-lived vibrational excitations in this region or due to a bath of excited phonons that perturb the $v=0\rightarrow1$ transition of these vibrations. The spectral signatures and the sub-picosecond to sub-nanosecond dynamics are identical, within experimental uncertainty, for both 1256 cm^{-1} and 1661 cm^{-1} excitation. This observation is consistent with the fact that both of these pump frequencies excite predominantly NO_2 stretching vibrations, thus eliciting a similar transient response and temporal behavior at other vibrations.

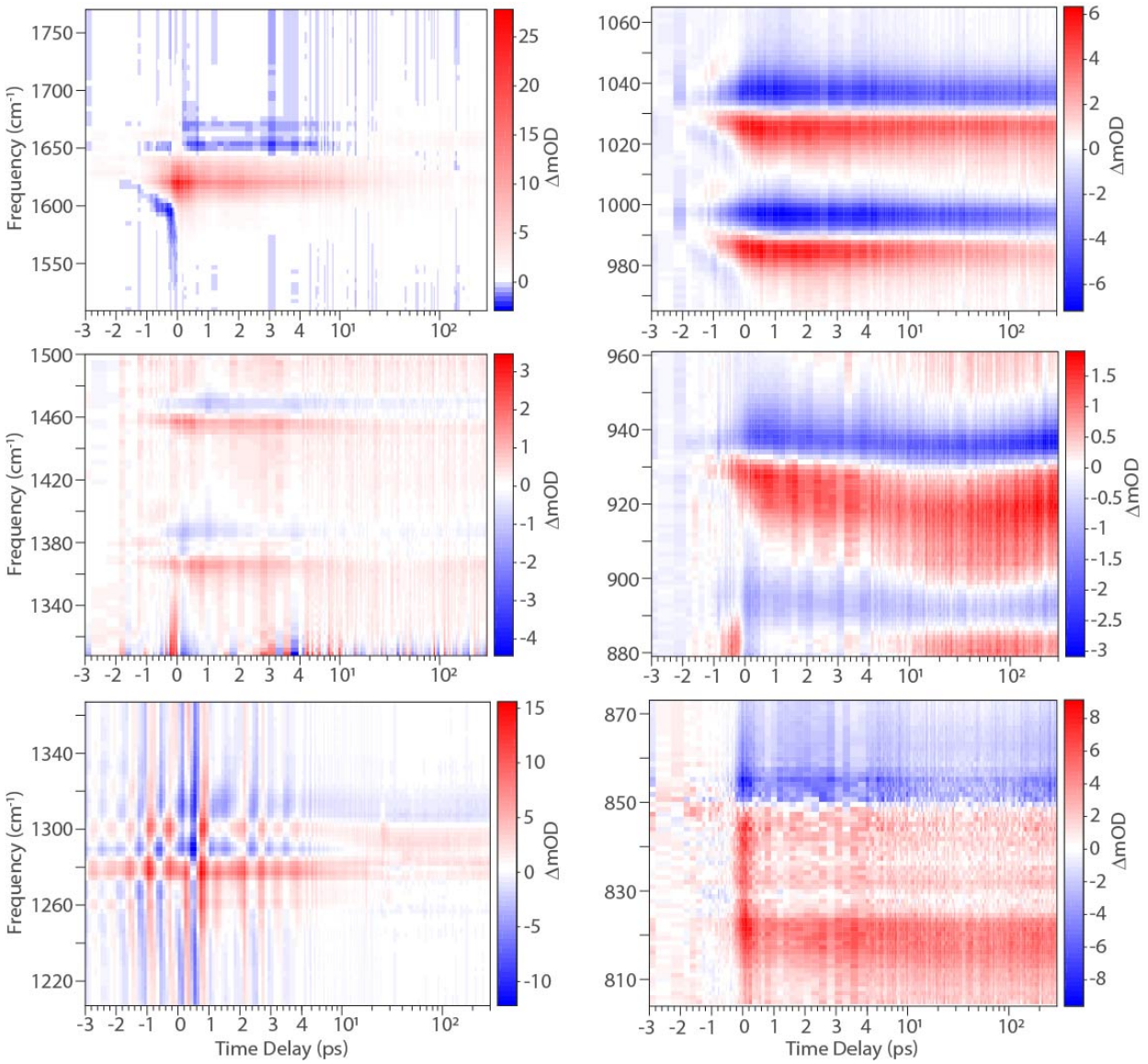

Figure 3-1. Transient infrared absorption spectra of PETN vibrations in the 800-1700 cm^{-1} region following narrowband excitation at 1256 cm^{-1}. Time delays are plotted on a linear scale until 4 ps, and on a logarithmic scale after.

Similar to the transient infrared response seen from 1661 cm^{-1} excitation, excitation of the 1040 cm^{-1} band that is characterized by alkyl skeletal vibrations also elicits a broad spectrum response at all IR-active modes below 1700 cm^{-1} at the earliest resolvable pump-probe time delay of 200 fs. Features above 850 cm^{-1} then see an intensification with a 0.5 ps time constant, except at 1300 cm^{-1}, where the signal weakens on this timescale. The sub-picosecond evolution is followed by an 8-10 ps decay of all features except the bands in the 900-940 cm^{-1} region. The 8–10 ps decay timescale agrees with lifetime of the 1660 cm^{-1} mode in the work of McGrane and co-workers that used Raman linewidths to approximate vibrational lifetimes.[13] The vibrational bands below 1000 cm^{-1} then display an σ(100 ps) evolution, consistent with observations from 1661 cm^{-1} excitation. A stark difference between the observations from the 1661 cm^{-1} or 1256 cm^{-1} excitation and the 1060 cm^{-1} excitation is seen in the 1280-1300 cm^{-1} region, which corresponds to the symmetric NO_2 stretching and alkyl skeletal vibrations. In this region, the 0.5 ps timescale is associated with a decay of the 1300 cm^{-1}

feature, concomitant with a rise in the 1280 cm^{-1} feature, possibly indicating a sequential or mode-dependent vibrational ladder climbing process. Furthermore, the bleach feature centered at 1315 cm^{-1} is much more pronounced relative to the neighboring bands following 1060 cm^{-1} excitation, suggesting that the vibrational coupling of the 1315 cm^{-1} mode with the 1040 cm^{-1} mode is stronger than with the 1660 cm^{-1} mode, and that VET from the 1040 cm^{-1} band involves a greater degree of participation from the mode at 1315 cm^{-1}. We note that the large oscillations in the degenerate frequency regions of Figures 3-1 and 3-2 are artifacts due to pump-probe interference.

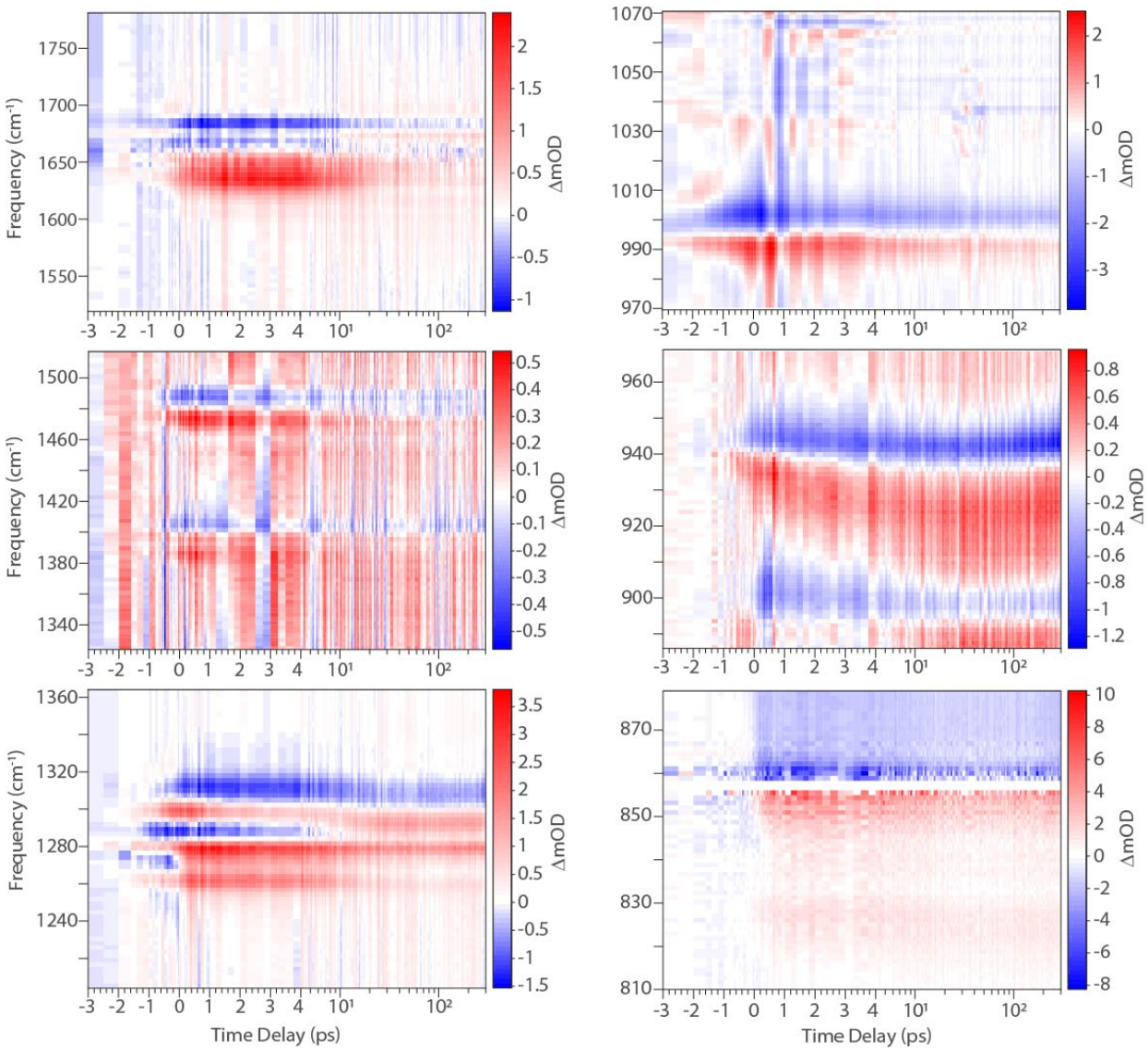

Figure 3-2. Transient infrared absorption spectra of PETN vibrations in the 800-1700 cm^{-1} region following narrowband excitation at 1060 cm^{-1}. Time delays are plotted on a linear scale until 4 ps, and on a logarithmic scale after.

3.1.2. Ab Initio Computational Results

A total of 121,452 unique displacements were made on the PETN ground state structure in order to construct the dynamical matrix needed for the third order force constants in the potential energy expansion. Much of the convergence testing on these DFT calculations was done on a simpler molecular crystal in nitromethane, suppressing the computational cost given the reduced atom count in these trial calculations. From these initial tests, we arrived at the following set of parameters for PETN: plane wave cutoff of 900 eV, energy convergence criterion of $1 \times 10e^{-8}$ eV, and a $3 \times 3 \times 3$ Monkhosrt Pack k-point mesh ($0.037 \times 0.037 \times 0.051$ $Å^{-1}$).[44-45] A Methfessel-Paxton scheme smearing width of 0.2 eV and the zero damping van der Waals corrections of Grimme[45-46] were applied for all calculations. Projector augmented wave pseudopotentials are used for each element species with an exchange-correlation functional of Perdew-Burke-Ernzerhof.[47] Input scripts are available upon request.

A displacement distance of 0.03 Å was found to be optimal to calculate force constants for nitromethane, and was subsequently used for all materials. This chosen distance has a subtle complexity about it that is specific to molecular crystals. For vibrations with a low stiffness (frequency), finite differences of the potential energy surface to produce force constants should be large enough (~0.1 Å) to yield a significant change in the energy, without leading to an excursion from the local minimum. In a much stiffer mode (higher frequency), the same displacement distance would result in excessively large changes in energy, which is numerically undesirable when calculating the same force constants. Since most crystals have a quite narrow (0-20 THz) phonon spectra, a single displacement distance for all modes is not a noteworthy approximation. However, in molecular crystals the phonon spectrum is considerably wider (0-100 THz), and a search for an optimal displacement was warranted.

The relaxed unit cell lengths of PETN-I were found to be $9.268 \times 9.268 \times 6.607$ Å, in agreement with previously published works.[48] From the harmonic portion of the potential energy expansion, the IR spectrum, one-phonon DoS, and normal modes of vibration can be extracted. By inspection of the normal mode displacements of the IR active modes, we have assigned peaks based on dominant atomic motions, see Table S1 in Ref. 18.

To inform on the VET process, we use the 2PhDoS to map out modes that are coupled to one another. As was detailed in Section 2.2.1, a Gaussian population perturbation was applied to a mode of our choosing, and the change in scattering intensity was recorded. These data are displayed in Figures 3-3 and 3-4 for the set of IR active vibrations in PETN. Noteworthy from the entire set of calculations is the density of possible scattering events throughout the 0-55THz spectra range, indicating that there are numerous active VET pathways for each perturbed vibration. Also of note is that the selection rules applied in Equation 4 and plotted here do not distinguish if there is a native vibration in the material that can "accept" a two-phonon scattering event into this frequency, hence the one-phonon and/or IR spectra are supplied to aid in this analysis. The data in green and purple are both the two-phonon density of states, but are separated by their classification as promotion or decay style of collision events, respectively.[24] The 2PhDoS data are inversely proportional to the lifetimes of these scattering events if each contributing scattering event is scaled by the cross-section of the colliding phonons; note that this scaling was not performed for the present results.

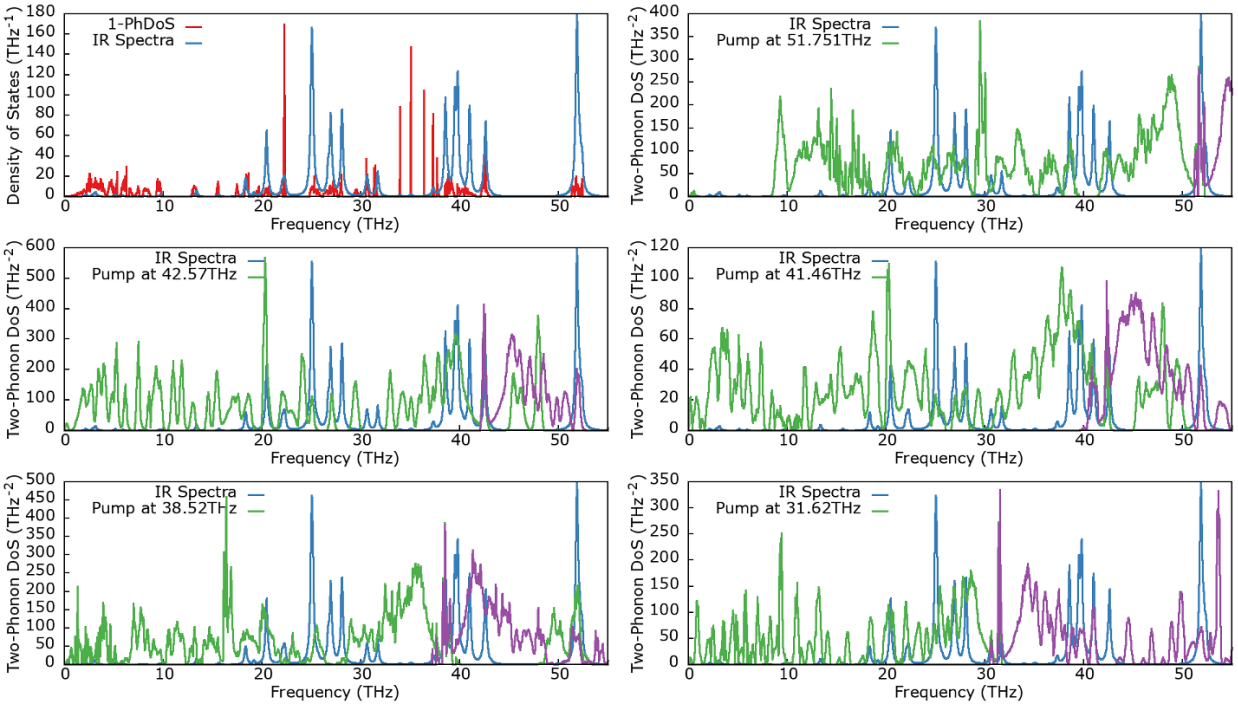

Figure 3-3. Composite two-phonon density of states in PETN for high frequency excitation

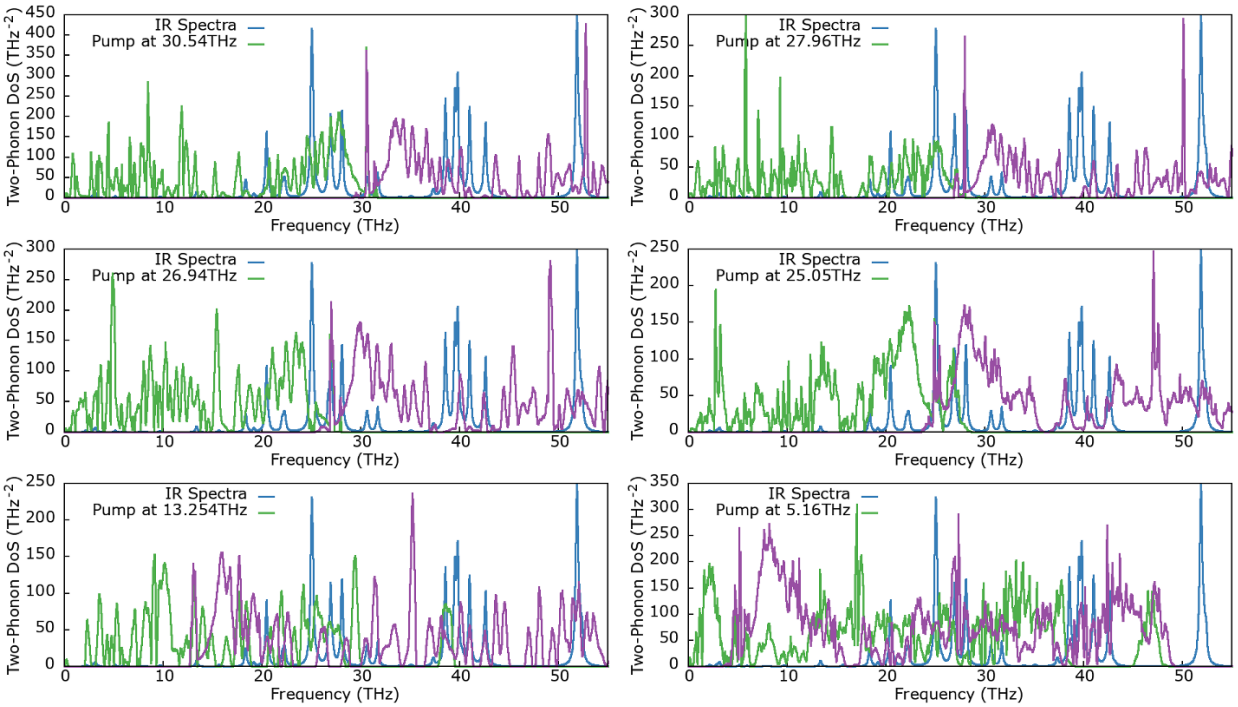

Figure 3-4. Composite two-phonon density of states in PETN for low frequency excitation

From the pumped asymmetric-NO stretch 2PhDoS (Figure 3-3 top-right), it was observed that there are no two-phonon collisions that include the lowest frequency vibrations in PETN(<8 THz). Similarly, where the pump is centered on 5.16 THz, displayed in Figure 3-4 bottom-right, there

are no scattering events that would directly excite the asymmetric NO stretch at 51.751 THz. This result is particularly interesting when considering that a strong compression of the lattice (*i.e.* a shock wave) creates an abundance of excited vibrations at low frequency (*ca.* <10 THz). Following phonon up-pumping theories, there thus needs to be additional intermediate scattering events that would delay the thermalization of these higher frequency intramolecular vibrations. The time delay from this energy cascade will ultimately affect the timescales associated with chemical reactions, where all of the predominant reaction paths depend on (uni-)intramolecular reaction coordinates. Regarding the intermediate scattering processes, the remaining data in Figures 3-3 and 3-4 demonstrate the numerous pathways of VET available in PETN. The dense 2PhDoS for all pump modes between 10 and 50 THz show that, regardless of the vibration of interest, there are two-phonon scattering events that are capable to shuttle energy to nearly all other vibrations in this same range. An exception needs to be made for the CH-stretch modes not plotted here, as their placement near 3000 cm^{-1} leaves very few scattering events that can scatter into these modes.

Surprisingly, and somewhat frustratingly, the calculated lifetimes were exceedingly small (or equivalently the linewidths are too large) when compared to previous Raman linewidth measurements.[13] Predicted lifetimes for PETN at 300 K ranged between 0.01 and 0.15 ps where they are expected to be 5-10 ps based on experimental linewidths; these small lifetimes were predicted for both PETN and Nitromethane. Calculation of these lifetimes is the (inverse of) product of two key terms, the 2PhDoS and a term that captures the scattering cross-section of each of the tallied phonon-phonon collisions. Since the 2PhDoS is simply tallying scattering events based on selection rules, we are led to believe the predicted scattering cross-sections is too large, resulting in the unexpectedly small lifetimes. The root cause is still unknown, but since excessively small lifetimes were not observed when we tested simple metals(Tungsten and Tungsten-Beryllium intermetallics) using the same protocol, the problem may be due to poor dispersion interactions captured within DFT resulting in modes that appear more strongly interacting than they truly are. Nonetheless, the set of DFT calculations were only intended in identifying VET pathways to be confirmed/denied by experiments, not for predicting the lifetimes of excited or coupled modes. For prediction of these properties, we turn our attention to the pump-probe setup of the MD simulations.

3.1.3. Molecular Dynamics Results

An important observation from the experimental effort was the distinct, and surprisingly long, timescales over which VET was still active. With these MD simulations, we aim to explain the mechanisms by which VET governed, and which sets of vibrations are active/inactive at each of these timescales. As was outlined in Section 2.2.2, the starting point of these simulations is to prepare the material in a vibrationally excited state (remember these are classical, not quantum excitations). Since the potential energy surface is different in MD as it is from DFT, the vibrational and IR spectra are subtly different as a result. While the mode character is the same (*i.e.* N-O asymmetric stretch), the exact frequency will be unique. For instance, the asymmetric-NO stretch band was observed to be centered at 1725 cm^{-1} from DFT, at 1660 cm^{-1} from experiment, and 1653 cm^{-1} from MD. The same protocol is used to select modes of interest, taking ones with the largest IR moment first. The mode character assignments are mostly the same for each of the selected IR active modes, but the set of frequencies studied with MD for PETN are 1653, 1329, 1238, 1193, 1102, 836, 538 and 253 cm^{-1}. Each target mode is individually coupled to a thermal bath at 1200 K, while the remaining vibrations in the system experience a thermal bath of 300 K. Pumped vibrations in practice wont achieve this target of 1200K because of coupling to other modes in the system which are held at a lower temperature. To ensure there a steady-state balance between energy input to the target mode and its' coupled vibrations, the system is held in this pumped state for 20ps, which is much longer than

experimental pump pulse durations. Depending on the resonator strength of the target vibration, anharmonicity and the density of neighboring vibrations the net temperature rise of the system will vary; the range of final temperatures was observed to be 386-461 K. Given the computational efficiency of MD, much larger samples than DFT are allowable. Here we use 6 × 6 × 6 supercell (>10k atoms) with a total of 4.1 ns simulated for each target mode.

Much like the analysis of the 2PhDoS, spectra of non-equilibrium states will be compared to a spectrum at thermal equilibrium. Herein, we assume that the system has reached a "complete" VET by 100 ps and the final spectrum taken at this time is considered as the equilibrium state. There are distinct advantages to using this self-contained equilibrium state, namely the pumped mode will elevate the temperature of the system, which will be unique for each target mode.

The time evolution of the total vibrational density of states is displayed in the top panels of Figures 3-5 through 3-7 along with the decay constant (middle) and pre-exponential factor (bottom) from a single exponential fit (*i.e.* $Ae^{(-x/B)} + 1$) to the normalized population data in the top panel. A pre-exponential factor greater than zero indicates that this mode is initially excited by, or coupled to, the target mode. Conversely, a value less than zero means this mode is initially de-coupled to the target mode and is depopulated relative to an equipartition of energy among modes. The time constant captures the relaxation or excitation of all modes as they return to an equipartition of energy at the pump elevated temperature. Fitted data that displayed greater than 25% relative error were omitted from the relaxation time plot.

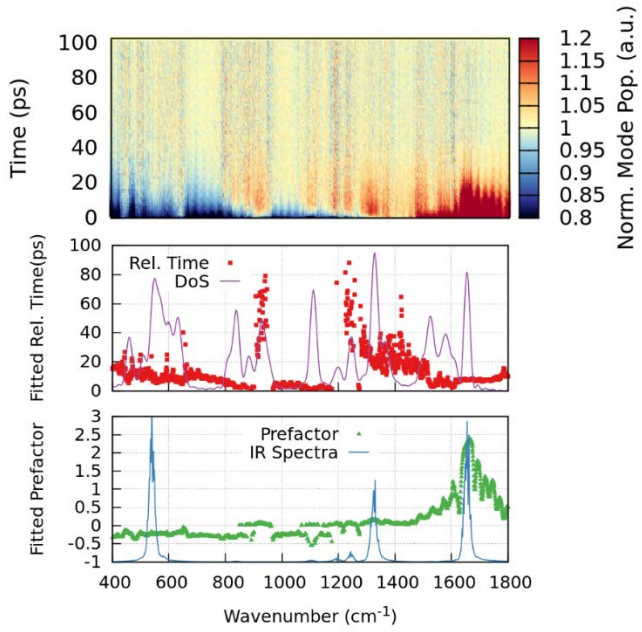

Figure 3-5. Molecular Dynamics results for VET in PETN where the asymmetric-NO stretch (1653 cm^{-1}) is pumped

The data shown in Figure 3-5 result from the band of asymmetric NO stretch modes coupled to the GLE thermostat. Initially, it is clear that the vibrations closest (1500–1700 cm^{-1}) to the thermostat resonance (1653 cm^{-1}) are most strongly out of equilibrium, having up to twice the kinetic energy than equipartition. Knowing that the system in isolation (after the thermostat is removed) is at 392 K implies that the target mode (again, in a classical sense) achieved a temperature of 784 K. Of course, temperature is ill-defined for a system far from equilibrium, but the analogy still holds here.

We observe a rapid (<10 ps) relaxation of the target mode while initially depopulated modes at very low frequencies (500-600 cm^{-1}) return to equilibrium on a slightly longer timescale (10-20 ps). This fitting process will not adequately capture any delayed dynamics based on a ladder-like VET process. For instance, vibrations at 1100 cm^{-1} in the top panel of Figure 3-5 show an initial de-population followed by a weak (~5–10%) excitation relative to the final 392 K spectra at a 100 ps delay. This non-exponential form of the dynamics results in a poor fit and decay constants close to zero. However, these delayed dynamics are hallmarks of the ladder-like VET processes that were also observed from experiments. The symmetric-NO stretch modes near 1330 cm^{-1} have interesting dynamics as well, they show a weak excitation (pre-factor ~0.2) but have much longer decay constants of 20-30 ps than the pumped asymmetric NO stretch modes. Given their similarity to the pumped mode, we would have assumed a strong initial excitation and similar dynamics, but it seems that the symmetric NO stretch modes play a key role in mediating energy transfer to lower frequency modes.

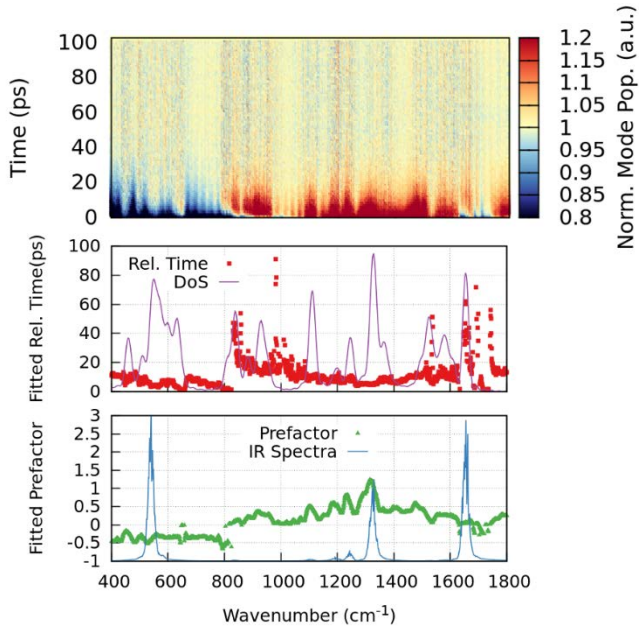

Figure 3-6. Molecular Dynamics results for VET in PETN where the symmetric NO stretch (1329 cm^{-1}) is pumped

Turning to the case where the symmetric-NO stretch modes are pumped, the data in Figure 3-6 displays the time evolution in the 400-1800 cm^{-1} spectral range and fitted constants to a single exponential decay function. In contrast to the asymmetric NO-stretch pump, a much wider set of vibrations are initially excited ranging from ~800 cm^{-1} to ~1700 cm^{-1}. Relaxation times of these anharmonically coupled vibrations seems to correlate with the frequency shift from the pumped mode, at the low end being equal to the expected <10 ps decay of the target mode. Conversely, the blue edge of the RO–NO_2 stretch, and C–C–H torsion modes (~850 cm^{-1}) show some of the longest decay times across all pumped modes tested. For completion of this proposed ladder process, the data of the pump coupled to the RO–NO_2 stretch, and C–C–H torsion modes is collected in Figure 3-7. Of note for this latter pumped mode is the apparent asymmetry in the nearby modes that are initially excited; the pre-factor data has a long tail above zero toward higher frequencies.

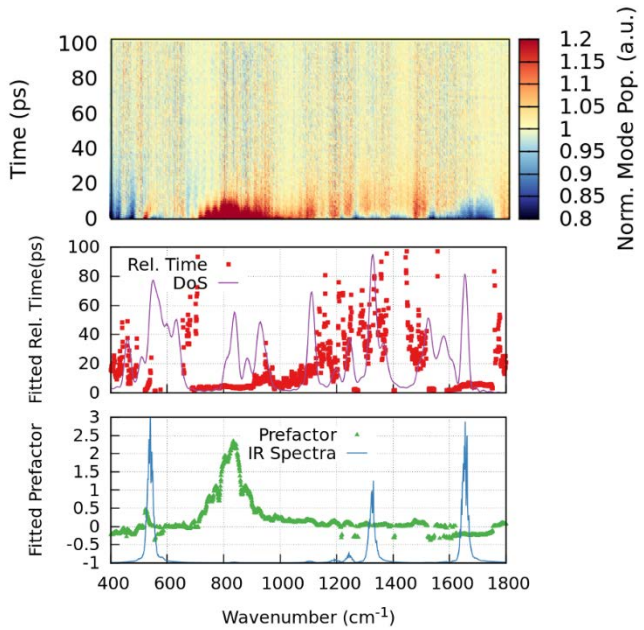

Figure 3-7. Molecular Dynamics results for VET in PETN where the RO–NO_2 stretch and C–C–H torsion modes (836 cm^{-1}) are pumped.

As was seen in experiments, there is a very rapid VET process in PETN due to many modes being anharmonically coupled to each other. This is seen in the middle panels of Figures 3-5 through 3-7, where large sections of the vibrational spectra are weakly excited by the GLE thermostat even where there is no direct coupling with the thermostat at these mode frequencies. Only the modes furthest down the VET ladder are de-coupled from the colored thermostat.

Across all of the tested target modes, we observe a rapid (<10 ps) relaxation of strongly coupled modes and a slight delay in VET completion for nearly all vibrations at around 20-30 ps. There are a few long lived excitations for a subset of target modes, the details of which will be analyzed for an upcoming publication. An important experimental observation that these MD simulations are still missing is the presence of longer-lived VET dynamics with σ(100 ps) timescales. It is hypothesized that these anomalously long timescale events are due to "hot-phonons" at frequencies <5 THz (well below the experimental detection limit) that continue to perturb and scatter into higher frequencies on the timescale of thermal conduction. To test this hypothesis with MD, we need to establish a non-equilibrium vibrational excitation (via GLE) that is also spatially localized. Up to now, the colored thermostat was applied homogenously throughout the bulk-like (periodic boundaries) crystal, negating any observation of thermal conduction through the sample. However, the "hot phonon" hypothesis can be tested after some adaptations to the simulation volume. In the spirit of the Müller-Plathe (MP) algorithm for establishing a steady thermal gradient in MD, we have adapted the method to replace one of the thermal reservoirs with a colored thermostat.[49] To recap this setup, standard MP simulations measure the thermal conductivity via Fourier's Law of a sample by periodically removing kinetic energy (atomic velocities) from one end of a rectangular cell and depositing it at the far end of the cell. Over time, this establishes a steady temperature gradient that is proportional to the thermal conductivity of the sample between the hot and cold reservoirs. However, we are not directly concerned with measuring the thermal conductivity, rather we need to benchmark our VET timescales against the timescale that a thermal gradient is destroyed after the constraints are lifted. This local thermal conduction timescale is the upper limit for the "hot-phonon" re-excitation hypothesis.

Thus, we performed another set of MD simulations to measure this thermal gradient destruction timescale; one simulation for a thermal gradient between two equilibrium reservoirs and a few simulations that have the hot reservoir replaced by a GLE thermostat. These simulations are significantly larger than the previous MD supercells, now a 5 × 5 × 40 replicas of the unit cell, with the thermal gradient established in the longest direction. In Figure 3-8, a thermal gradient is established over the first two nanoseconds after which the thermostats are removed, and the gradient is slowly destroyed via conduction. Functionally, we again assume this relaxation takes on an exponential decay. The equilibrium thermal gradient case displayed a 16.4 K/nm initial gradient that decays with a time constant of 298.5 ps. Whereas an asymmetric-NO stretch pumped thermal gradient shown an initial gradient of 5.8 K/nm with decay constant 318.4 ps. For comparison to either of these cases, a colored thermostat coupled to the mode at 253 cm^{-1} in PETN had an initial gradient of 15.0 K/nm and decay constant of 316.8 ps. All of these data, along with the associated fits, are plotted in Figure 3-8. Of note is that the non-equilibrium (defined as a non-equipartition of energy) thermal gradient where high frequency modes are excited shows a longer decay time than the two equilibrium cases, presumably due to the extra VET processes needed to shuttle this excitation energy down into low frequency, heat carrying phonons. The assumption of low frequency modes being the dominant heat carriers is due to their large mean free paths and group velocity relative to intra-molecular vibrations with very small dispersion and thus small group velocity. A proof of this assumption would involve taking spectra from sample volumes between the hot and cold reservoirs looking for excited NO stretch vibrations where there is no thermostat applied. We have not done this analysis at the time of writing this report, but it will be included in an upcoming publication.

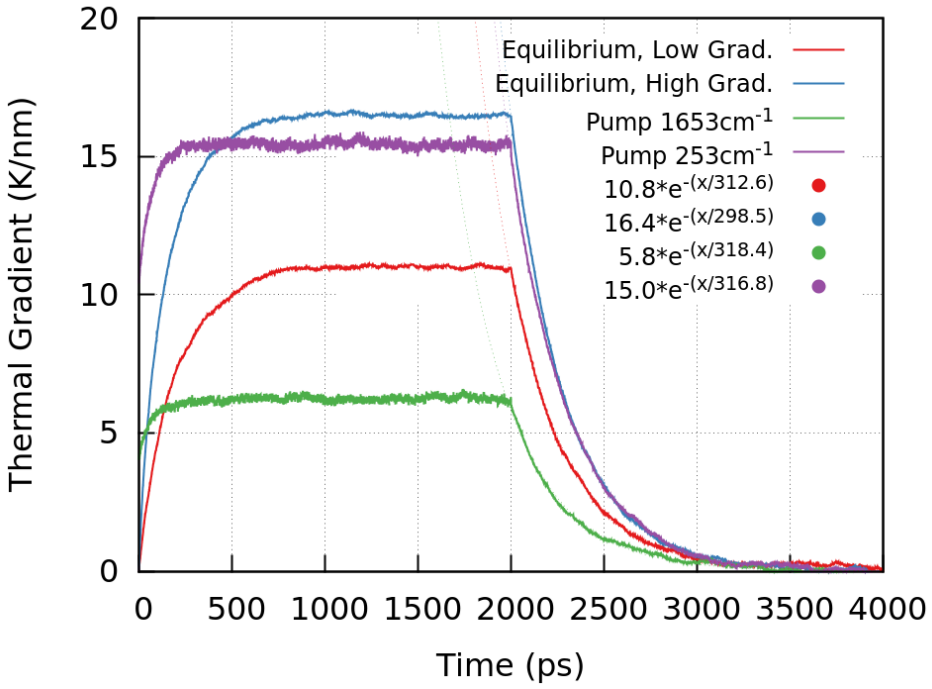

Figure 3-8. Molecular Dynamics results for (non-) equilibrium thermal conduction in PETN

Following the local thermalization of high frequency vibrations, we must assume up-pumping from phonons is still active on the ~300 ps timescale while heat is being conducted away. It is possible that the 'noise' we see at time delays >50 ps in the top panels of Figures 3-5 thru 3-7 are due to broadening and shifting of modes affected by this 'hot-phonon' bath. Looking back on the DFT

predicted 2PhDoS in Figures 3-3 and 3-4, there are several scattering events that involve these low frequency modes that can reach into higher parts of the PETN vibrational spectrum. Re-iterating the shortcomings of the DFT results, a true test of these up-pumping events would be if proper scattering cross-sections can be calculated. Through this work we have built the necessary code connections between LAMMPS and PhonoPy to allow for third-order force constants to be calculated from an interatomic potential, but there are additional data- and memory-management challenges that need to be surmounted. We have tested these code developments on simpler materials, the challenging part is due to the atom counts and complex crystal structures that these molecular solids display. This code is available on GitHub via https://github.com/mitwood/phono3py , documentation of the changes and merge into upstream repositories forthcoming.

3.2. 1,3,5-Trinitroperhydro-1,3,5-Triazine (RDX)

3.2.1. Femtosecond Infrared Spectroscopy Results

Figure 3-9 shows the infrared transmission spectrum of the ~2.5 μm thick film of RDX deposited on 1 mm thick CaF_2 windows used in our experiments. Vibrational mode assignment of the infrared bands is performed based on Ref. 50. The C-H stretching vibrations appear in the 3000 cm^{-1} region and the NO_2 stretch vibrations comprise the bands at 1570 and 1600 cm^{-1}. The absorption features at 1275, 1390, 1435 cm^{-1} correspond to CH_2 twisting, wagging and bending vibrations with the N-N stretching vibration contributing to the 1275 cm^{-1} peak as well. The bands at 1040 and 1220 cm^{-1} correspond to the N-C stretching vibration. The mode at 950 cm^{-1} corresponds to the N-N stretch and CH_2 vibrations, while the band at 880 cm^{-1} corresponds to the C-N stretch, CH_2 rock and N-N stretch vibrations. N-N stretching and NO_2 scissoring vibrations contribute to the band at 840 cm^{-1}.

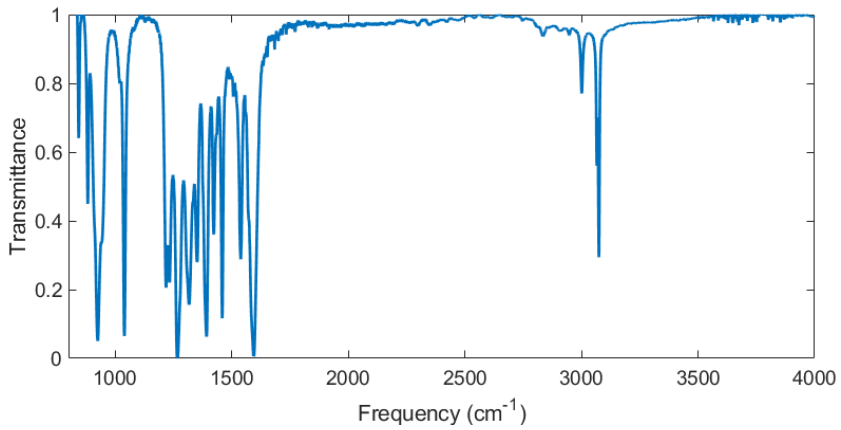

Figure 3-9. Infrared spectrum of ~2.5 μm thick film of RDX on a 1 mm thick CaF_2 window.

Figure 3-10 shows the time-resolved infrared absorption spectra following narrowband excitation at 1533 cm^{-1}, corresponding to pumping the NO_2 stretching vibrations. Similar to PETN, instantaneous bleaching is observed at all infrared active vibrations within the instrument time resolution of 200 fs, indicating strongly coupled vibrations in RDX. The sub-picosecond dynamics are followed by dynamics on σ(1 ps) timescale at all infrared transitions. This σ(1 ps) timescale in RDX almost universally corresponds to an evolution towards broadened and red-shifted vibrational

lineshapes, which manifest in transient infrared spectra as induced absorption features on high and low frequency sides of a bleach feature; such lineshapes are a hallmark of the influence thermal or non-thermal phonon distributions exert on high frequency vibrations.[13, 18] This evolution is particularly evident for vibrations in the 1200–1600 cm^{-1} region, at 1040 cm^{-1}, and in the 800–900 cm^{-1} region, where the infrared bands are well-separated allowing clear visibility into the broadening and shifting of peaks past 10 ps. While vibrations in the 1300–1400 cm^{-1} region do not show notable dynamics past 10 ps, as displayed in Figure 3-11, features at 1600, 1455, 1270, 1040, 935 cm^{-1} clearly and monotonically evolve with an σ(100 ps) time constant. The spectral assignments based on Ref. 50 suggest that the vibrational frequencies that display σ(100 ps) evolution correspond to NO_2 stretching, N-N stretching and N-C stretching vibrations, while the 1300–1400 cm^{-1} features that do not show a clear σ(100 ps) dynamics are assigned to CH_2 vibrations. The low signal level below 1000 cm^{-1} precludes a firm conclusion on the long-time evolution of the signal. Many of these observations are similar to those in PETN,[18] where the most pronounced change in signal amplitude occurs on sub-picosecond to σ(1 ps) timescales, while evolution of certain vibrations on the σ(100 ps) timescale mostly involve more subtle changes to the signal amplitude and peak position.

The observed dynamics in RDX suggest that the instantaneous appearance of bleach features due to strong vibrational coupling is followed by VET on the σ(1 ps), which at every step, excites low frequency phonon vibrations. The excited phonon vibrations in turn perturb the probed high frequency vibrations, thus prompting shifts and broadening of the infrared features that are generally akin to difference infrared spectra of the sample at elevated and at room temperatures.[18] However, the σ(100 ps) evolution of many vibrational transitions suggests that the probed volume of the sample has not reached thermal equilibrium even by the longest measured time delay of 300 ps, indicating that VET is still occurring on these long, hundreds of picosecond timescales. The vibrations at the above-mentioned frequencies that noticeably display the σ(100 ps) evolution (*i.e.* the NO_2, N–N, N–C stretching modes) are those whose frequencies are sensitive to phonon-induced perturbations to local environment, compared to the CH_2 vibrations in the 1300–1400 cm^{-1} region that are relatively inert to local environment and do not show obvious σ(100 ps) dynamics. Indeed, such mode-specificity hints that a shock-excited phonon bath may more easily couple to these labile reaction coordinates. While some of these observations and interpretation mirror those in PETN, a key difference between results in RDX and PETN is that the σ(10 ps) evolution at all probed vibrations is nearly absent or rather insignificant. A possible explanation is that multiple σ(1 ps) VET steps could be operating in parallel in RDX, whereas multiple sequential σ(1 ps) VET steps were hypothesized to result in an effective σ(10 ps) evolution in PETN.[18]

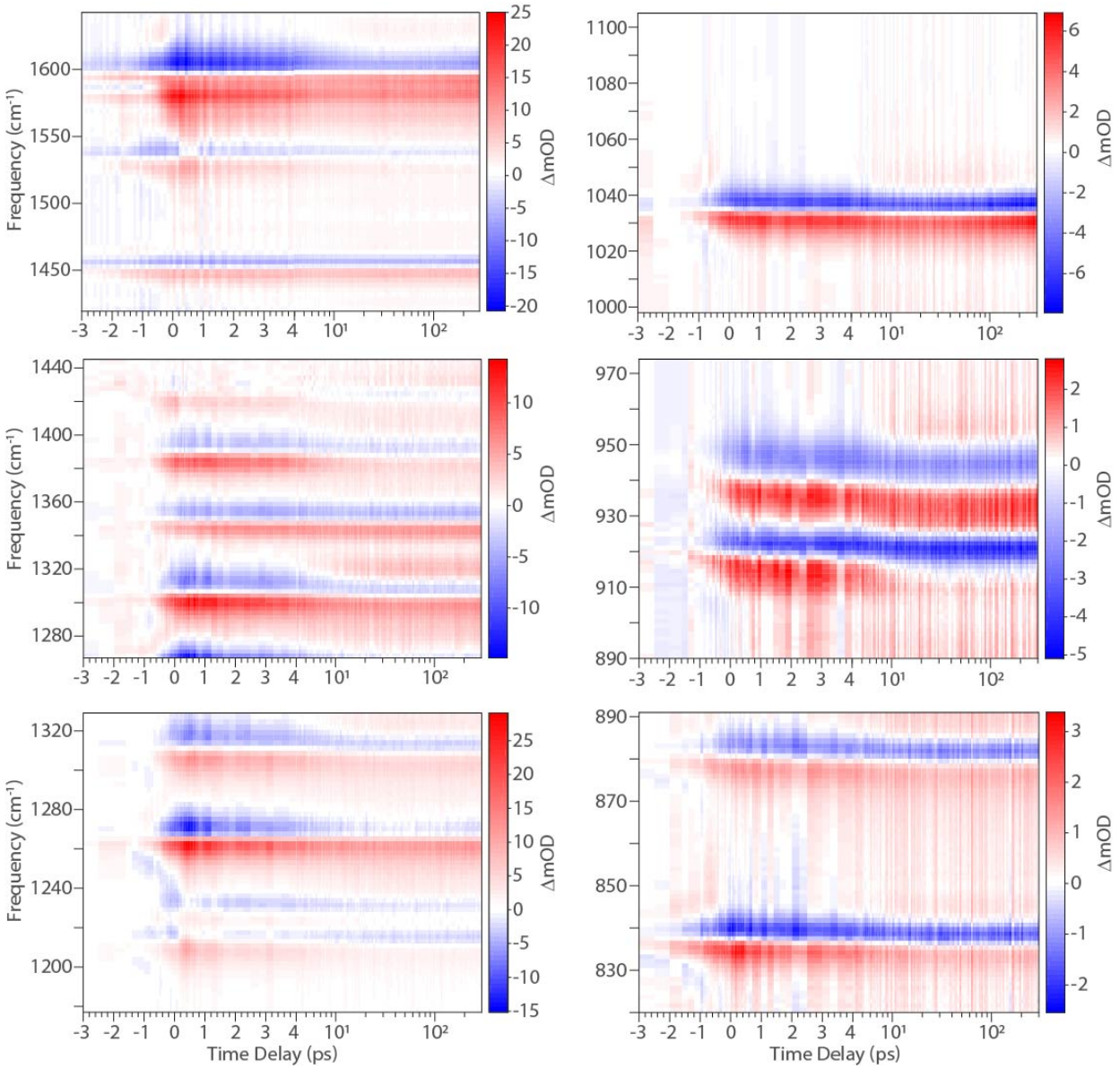

Figure 3-10. Transient infrared absorption spectra of RDX vibrations in the 800-1700 cm^{-1} region following narrowband excitation at 1533 cm^{-1}. Time delays are plotted on a linear scale until 4 ps, and on a logarithmic scale after.

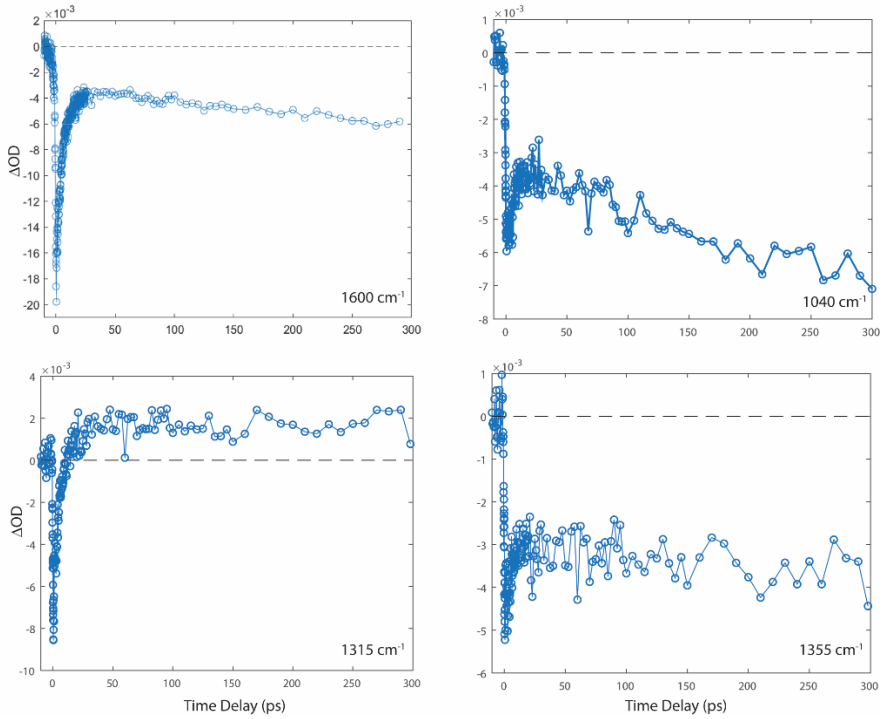

Figure 3-11. Lineouts through the transient infrared spectra of RDX at the indicated frequencies.

3.2.2. Ab Initio Computational Results

A total of 51,642 unique displacements were made on the RDX ground state structure in order to construct the dynamical matrix needed for equation 4 of Ref. 26. A plane wave cutoff of 900 eV with a k-point spacing of 0.039 × 0.029 × 0.032 $Å^{-1}$ was used for a unit cell of alpha-RDX (contains 168 atoms). Additional VASP settings are the same as what was used for PETN, including the same pseudopotentials. All VASP simulations were run on Sandia computing clusters utilizing up to 200 nodes at a time. In order to schedule the tens-of-thousand individual jobs, asynchronous tile evaluation from the DAKOTA optimization software is utilized.[51] DAKOTA thus allows a single, large allocation of compute nodes to distribute the individual VASP jobs to idle nodes and queue up tasks until the full batch of jobs is completed (while not the intended use of DAKOTA, it works in our favor here). It is important to stress the ground-breaking scale of these calculations, as nearly all previous work studying the thermal properties of materials from this direct potential energy expansion only total a few hundred DFT calculations at a time. In order to resolve long wavelength deformations of the crystal, supercell geometries are typically used, but this is prohibitively expensive given the unit cell of RDX already contains 168 atoms and cubic scaling of the computational cost of DFT.

As was the focus in section 3.1.2, the prediction of the 2PhDoS is desired to understand the VET pathways in RDX. Results collected in Figure 3-12 show the VET pathways from the asymmetric-NO stretch (middle panel) and the symmetric-NO stretch modes, while the top panel displays the IR spectra and one-phonon density of states. Plotted are the 2PhDoS difference between the nominal, thermally occupied Bose-Einstein populations at 300 K and where a Gaussian perturbation of unit height and 2THz width is added at the vibration of interest. Similar to the PETN 2PhDoS, there are a large number of scattering events that include both of these NO stretch modes, indicating rapid VET. At the time of writing this report, the dynamic VET simulations utilizing the method outlined in Section 2.2.2 have yet to be analyzed.

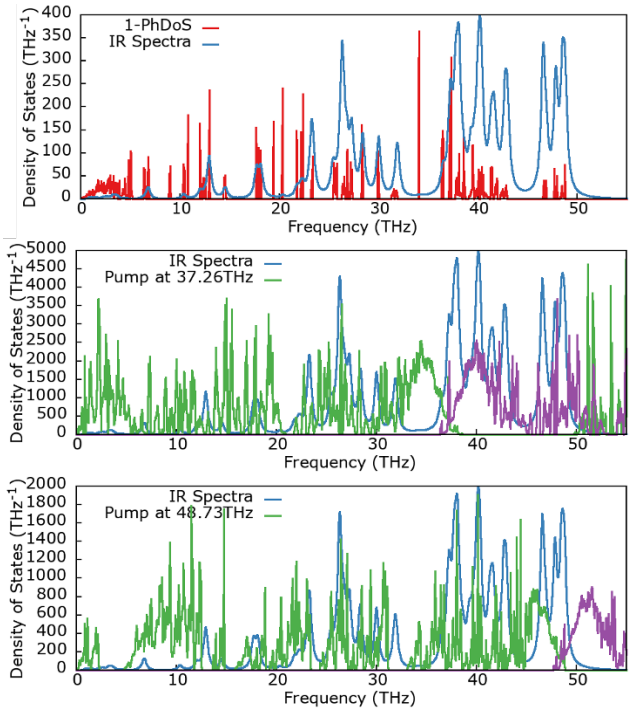

Figure 3-12. Composite two-phonon density of states in RDX for high frequency excitations

3.3. 2,4,6-Triamino–1,3,5-Trinitrobenzene (TATB)

3.3.1. Femtosecond Infrared Spectroscopy Results

Figure 3-13 shows the infrared transmission spectrum of ~2.5 μm thick film of TATB deposited on a 1 mm thick CaF_2 window. Assignments are performed using Ref. 52. The bands near 3200 cm^{-1} are due to the symmetric and asymmetric stretching vibrations of the NH_2 groups. The 1600 cm^{-1} feature is due to the C–NH_2 stretch and the NH_2 bending motion. The features between 1460 and 1490 cm^{-1} comprise NH_2 bending, rocking, scissoring, and ring twisting vibrations. The low frequency vibrations between 800 and 1400 cm^{-1} are assigned to vibrations involving predominantly the NH_2 groups (twist, wag, rock). The modes at 1340, 1173, 1160, and 1030 cm^{-1} also involve the C–NO_2 stretching vibration, while the band at 1225 cm^{-1} has contribution from the C–NH_2 stretching vibration. Unlike in PETN and RDX, the only band with NO_2 stretching character is located at 1160 cm^{-1}. We note that some of the TATB absorption features saturate; however, experiments on RDX comparing thick (with saturating absorptions) and thin samples yielded consistent dynamics and trends.

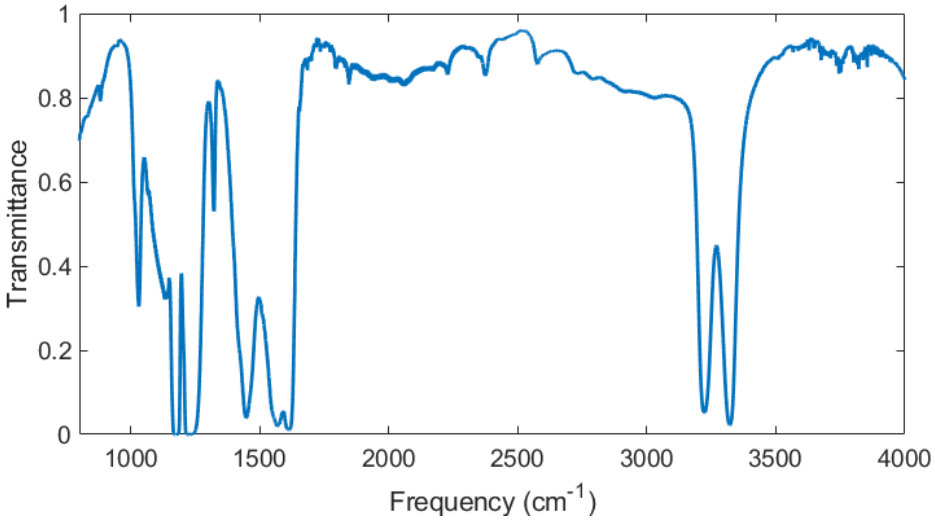

Figure 3-13. Infrared spectrum of ~2.5 μm thick film of TATB on a 1 mm thick CaF_2 window.

Figure 3-14 shows time-resolved infrared absorption spectra following narrowband pumping at 1533 cm^{-1} that leads to the excitation of the C–NH_2 stretching and NH_2 bending vibrations. This excitation elicits a bleach response from the NH_2 stretching vibrations near 3200 cm^{-1}, as well as from all other infrared-active modes in the range of frequencies probed, within the ~200 fs time resolution of this experiment. This again supports the idea that, similar to PETN and RDX, infrared-active vibrations in the mid-infrared region of TATB are strongly coupled. This ultrafast response includes an immediate and surprising appearance of induced absorption features on the *higher* frequency side of bleach features, such as at 3400 cm^{-1} and 1640 cm^{-1}. While induced absorption on the *lower* frequency side of bleach features are common in femtosecond transient infrared absorption spectroscopy due to the anharmonically red-shifted v=1→2 transitions caused by the interaction of the probe pulse with the sample, induced absorption on the higher frequency side of a bleach feature is anomalous. Given that there are no neighboring transitions at higher frequencies of the infrared bands in the 3200 and 1600 cm^{-1} regions that could cause the induced absorptions at 3400 cm^{-1} and 1640 cm^{-1}, the prompt appearance of induced absorption at 3400 and 1640 cm^{-1} suggests instantaneous broadening of the NH_2 stretching, C–NH_2 stretching and NH_2 bending vibrational lineshapes.

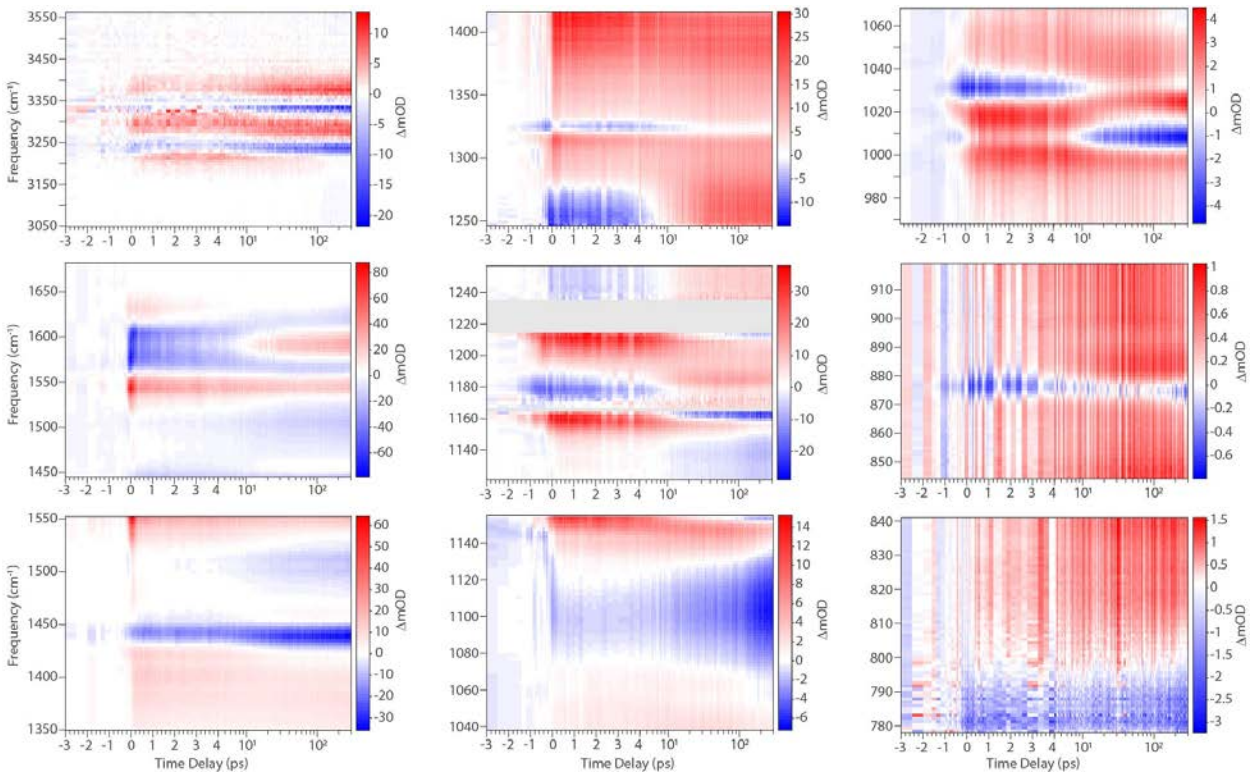

Figure 3-14. Transient infrared absorption spectra of TATB vibrations in the 800-3500 cm^{-1} region following narrowband excitation at 1533 cm^{-1}. Time delays are plotted on a linear scale until 4 ps, and on a logarithmic scale after.

Subsequent to this ultrafast response, an σ(1 ps) to σ(10 ps) evolution occurs at all infrared transitions. In the 3200 cm^{-1} region, at 1505 cm^{-1}, 1440 cm^{-1} and 1100 cm^{-1}, this timescale corresponds to an intensification of the bleach features, whereas it corresponds to the decay of bleach features in the 1600 cm^{-1} region, at 1325 cm^{-1}, 1250 cm^{-1}, 1180 cm^{-1}, 1030 cm^{-1} and 880 cm^{-1}. Figure 3-15 displays lineouts at some of these frequencies. These dynamics then give way to slower σ(100 ps) evolution of the majority of infrared transitions in TATB, involving highly pronounced shifts, broadening and changes in signal intensity. In the 3200 cm^{-1} region and at 1440 cm^{-1}, the broadening of the two features intensifies, while the transitions at 1606 and 1575 cm^{-1} experience significant shifting and possible broadening. The 1325 cm^{-1}, 1180 cm^{-1}, and 1030 cm^{-1} features shift to lower frequencies and broaden – a behavior that mirrors the effect of phonon excitations on high frequency vibrations.[18] However, the long-time behavior at these latter frequencies involves a change in sign from bleach to induced absorption, which then further evolves with a σ(100 ps) time constant. The bleach feature at 1250 cm^{-1} undergoes a remarkable change in the sign of the signal, without clear evidence for shifts or broadening. The weak shoulder to the low frequency side of the 1030 cm^{-1} peak, at ~1010 cm^{-1}, shows a bleach at time zero, but proceeds to evolve into an induced absorption, which decays on a σ(1 ps) to σ(10 ps) timescale, and then turns into a negative absorption feature that further intensifies on a σ(100 ps) timescale. The signal centered at 1100 cm^{-1} does not flip sign, but instead shows a very pronounced intensification of signal as well as significant broadening on long time scales. Features at 880 cm^{-1} and near 785 cm^{-1} also show pronounced σ(100 ps) time scale evolution.

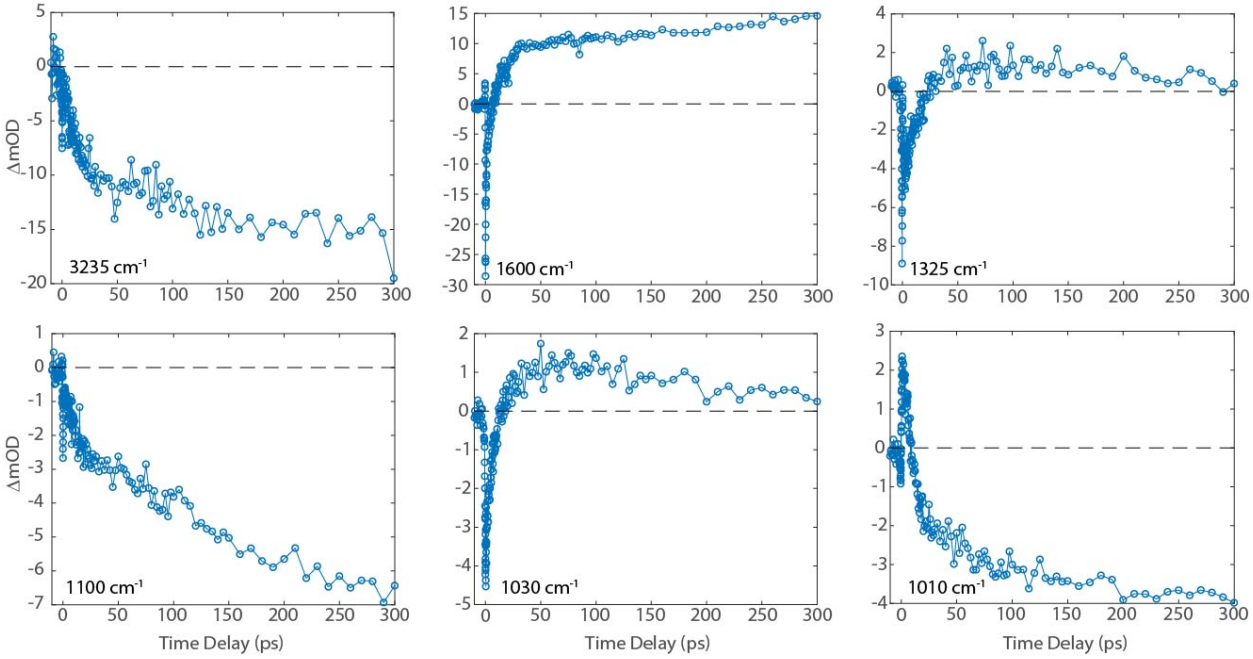

Figure 3-15. Lineouts through the 1533 cm^{-1}-pumped transient infrared spectra of TATB at the indicated frequencies.

Excitation of TATB at 1190 cm^{-1}, corresponding to the excitation of predominantly C-NO_2 stretching vibration, results in transient infrared spectra and temporal behavior that closely mirror results from 1533 cm^{-1} excitation, as shown in Figure 3-16. These results also show sub-200 fs response, followed by σ(1 ps), σ(10 ps), and σ(100 ps) dynamics. The long-time behavior is as stark, with pronounced changes to center frequencies, linewidths, and signal intensities. The one notable difference is in the 3200 cm^{-1}, where the induced absorption at 3400 cm^{-1} grows in on the σ(1 ps) timescale, rather than appear near time-zero as seen with 1533 cm^{-1} excitation. This difference suggests that the NH_2 stretching vibrations do not experience broadening immediately following 1190 cm^{-1} excitation.

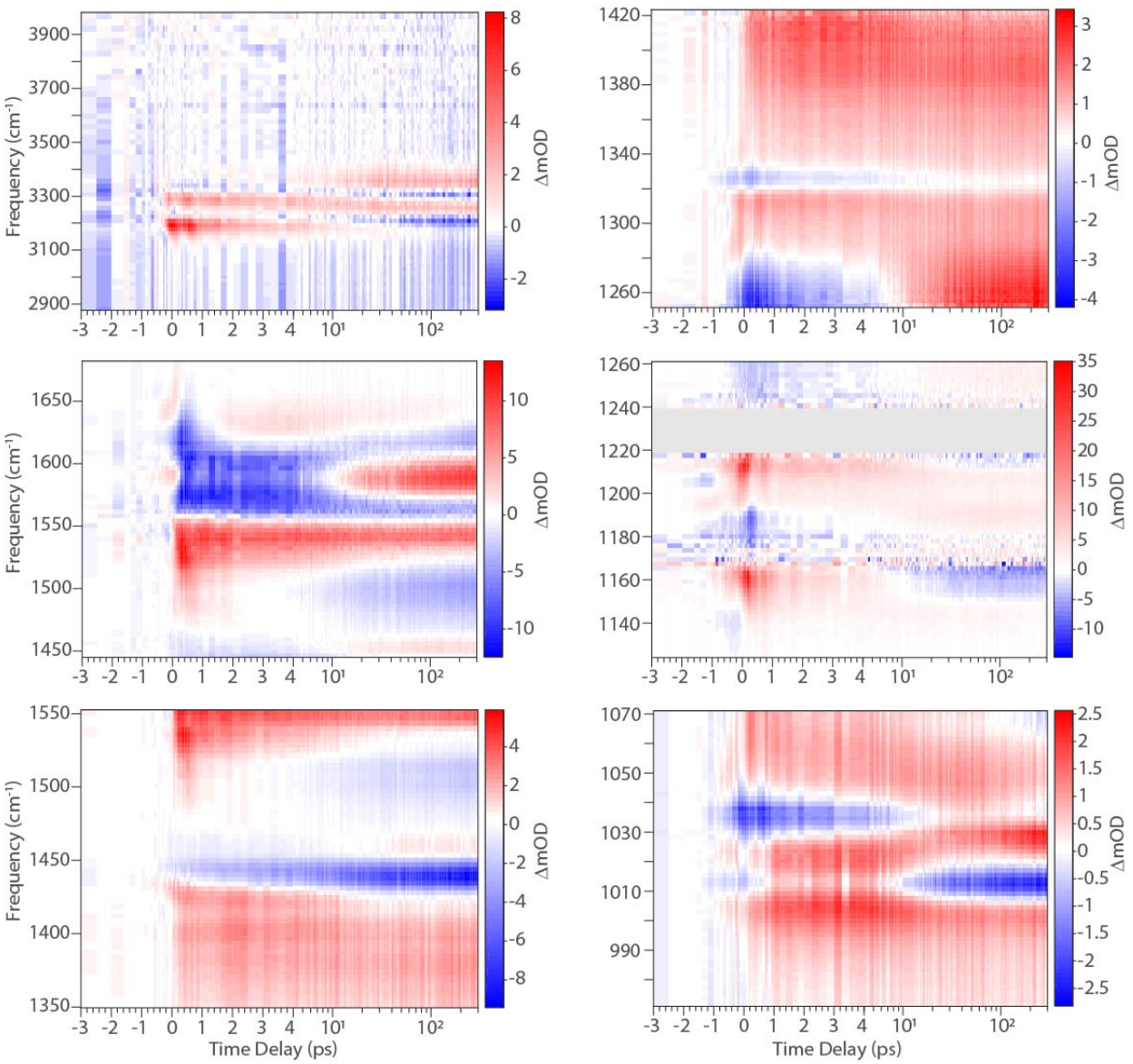

Figure 3-16. Transient infrared absorption spectra of TATB vibrations in the 800-3500 cm^{-1} region following narrowband excitation at 1190 cm^{-1}. Time delays are plotted on a linear scale until 4 ps, and on a logarithmic scale after.

While the sub-picosecond, σ(1 ps) and σ(10 ps) dynamics in TATB show interesting trends and very rich dynamics that require further analysis and interpretation, the pronounced σ(100 ps) behavior of transient features in TATB compared to much more subtle spectral evolution in RDX and PETN on this timescale suggests significant differences in the coupling of TATB molecular and phonon vibrations. The conspicuous changes to the vibrational lineshapes on the σ(100 ps) timescale as well as the instantaneous broadening of certain high frequency infrared lineshapes in TATB indicate strong vibration-phonon or vibration-vibration coupling that considerably modifies the transition energies and infrared linewidths during VET. Further analysis of experimental data is underway to enable comparisons with MD simulations presented below, and to achieve a deeper understanding of the observed dynamics and their implications on VET in TATB.

3.3.2. Molecular Dynamics Results

All MD simulations of TATB utilized the non-reactive interatomic potential of Kroonblawd *et al.*[31] which has demonstrated superb accuracy with respect to experiments for mechanical and thermal properties. In addition to the two-, three- and four-body bonds of the other IAP used herein, this IAP adds an additional long-range, pair-wise, term that captures the hydrogen bonding interactions in TATB. A 6 × 6 × 6 replica (~10k atoms) of the unit cell is equilibrated at 300 K and 1atm of pressure for 125 ps prior to gathering any spectra. In order to capture the N-H modes at ~3500 cm^{-1} the sampling frequency used in equation 5 had to be lowered to 4 fs. As with PETN, a set of IR active vibrations were chosen for the GLE pump-probe simulations, these were (not in order of IR intensity) 1634, 1322, 1223, 940, 880, 672 and 497 cm^{-1}. A detailed mode assignment from DFT/MD was not completed at the time of writing this report. Final temperatures of all pump-probe MD simulations were between 384 K and 429 K. The full vibrational density of states and calculated IR active modes are given in the middle and bottom panels of Figure 3-17, respectively.

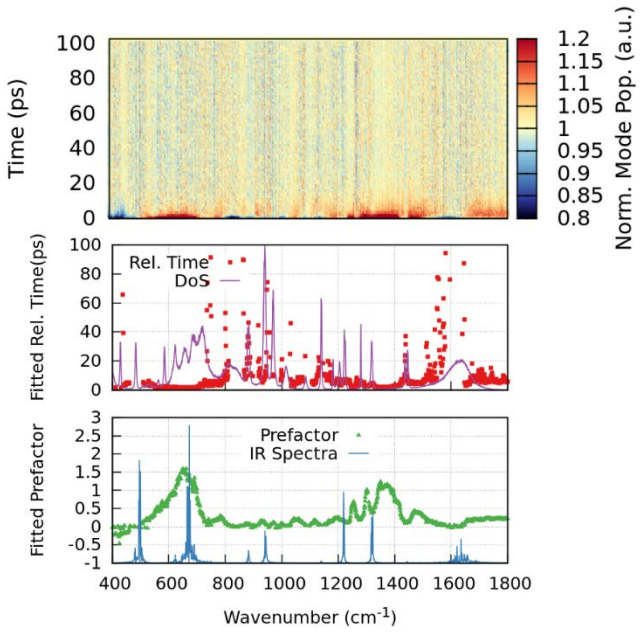

Figure 3-17. Molecular Dynamics results for VET in TATB where the vibrations centered on 672 cm^{-1} are pumped.

Globally, TATB displays much faster VET dynamics than PETN. An example of this observation is given in Figure 3-17 where a thermostat is coupled to the vibration at 672 cm^{-1}. Shortly after the thermostat is removed (t=0 ps), the initially excited modes relax to a population equivalent to that at a time delay of 100 ps (same normalization scheme as PETN). Fitted exponential decay constants (Figure 3-17 middle panel) to the pumped mode show a <5 ps lifetime for all modes initially anharmonically coupled to the pumped mode. Interestingly, there is strong coupling between the pumped modes at 672 cm^{-1} and those between 1200-1400 cm^{-1}, with the fitted pre-factor data (Figure 3-17 bottom panel) showing a preferential excitation of IR-inactive mode at 1282 cm^{-1} over the nearby and IR-active 1319 cm^{-1} and 1224 cm^{-1} vibrations. None of these anharmonically coupled modes are long lived, with fitted lifetimes <5 ps as well.

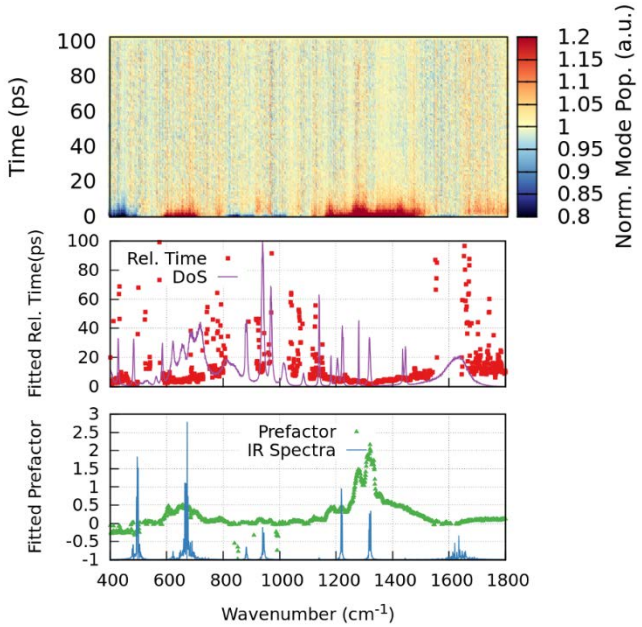

Figure 3-18. Molecular Dynamics results for VET in TATB where the vibrations centered on 1323 cm^{-1} are pumped.

Looking at the inverse of this excitation process, Figure 3-18 collects the spectral evolution and fitting constants of TATB pumped at 1323 cm^{-1}. While this 1323 cm^{-1} pumped mode couples to lower frequency modes at nearly half its frequency, the fitted pre-factor data (Figure 3-18, lower panel) also displays a long tail toward higher frequency modes which covers the red edge of the N-H modes clustered around 1600 cm^{-1}. Much of the "long-lived" excitations that are on display in the fitted relaxation time data are fictitious and the result of weak initial excitations/depopulations, it is always best to look first for non-zero pre-factors and interpret those relaxation times. More MD results are available upon request.

To speculate, the relatively rapid VET in TATB arises from planar geometry of the TATB molecule. It may be that each of the studied intra-molecular pumped modes interacts strongly with other in-plane (*e.g.* crystallographic, multi-molecular planes) vibrations, which are extended over many molecules; a similar explanation offered by Ostrander et al.[14] where N-O stretch modes in PETN were found to be multi-molecular in nature. Given the strong, planar, hydrogen bond network found in TATB, such delocalization may be responsible for a similar response seen here. It is thus worth checking for strong coupling of these pumped intra-molecular modes to the low frequency phonon modes (<400 cm^{-1}), which would be the assumption if these modes are delocalized.

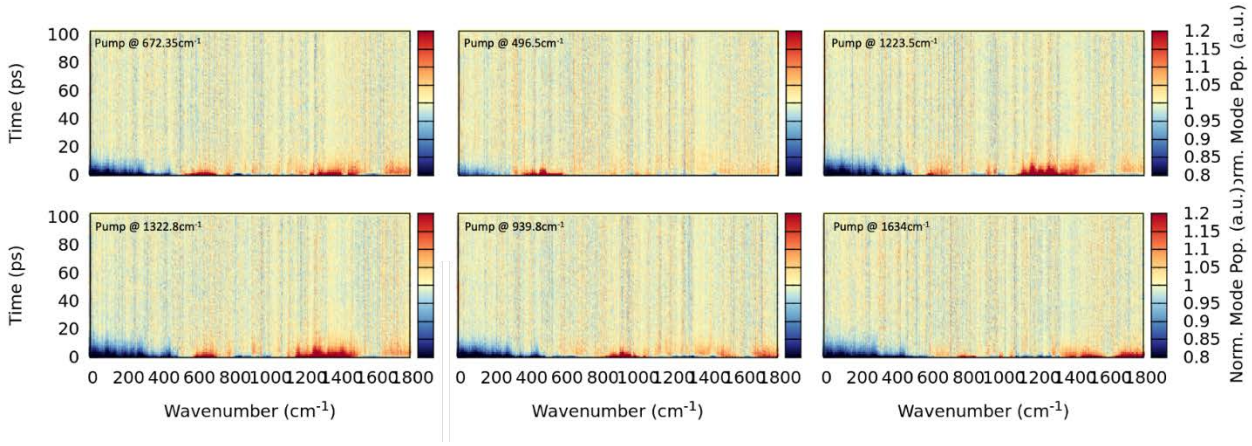

Figure 3-19. Composite Molecular Dynamics results of the spectral evolution in TATB pumped at various indicated frequencies.

To highlight the behavior of low-frequency modes, Figure 3-19 collects the spectral evolution of all pumped modes in TATB. It is observed that low frequency phonon modes are universally under populated relative to the equilibrium spectra at the end of the simulated time. Interestingly, these modes relax to the equilibrium population on a ~10–20 ps timescale which is slightly longer than the fast VET among intra-molecular vibrations. To reiterate, a normalized population less than one means these vibrations are "colder" than the final spectra, which is elevated due to the pumped mode. For example, if there is no coupling between these cold modes and the pumped mode, then they will exhibit a temperature of 300 K while the final normalizing spectra is known to be between 384 K and 429 K. Since the total kinetic energy is the same in both the initial and final spectra, these low frequency phonons are thus interpreted as depopulated. All of this suggests that the rapid, <5 ps VET observed among intra-molecular vibrations cannot be solely attributed to strong coupling to a low-frequency bath of modes. Follow on simulations characterizing the thermal conduction timescale, as was done in PETN, are needed to probe the ~100 ps evolution of features observed in experiments.

4. CONCLUSIONS

This report presents our investigation of vibrational energy transfer dynamics in three energetic materials that exhibit different sensitivities to a shockwave impulse – PETN, RDX and TATB. Our approach leveraged the combination of three unique capabilities at Sandia National Laboratories: (1) femtosecond broadband infrared spectroscopy, which allowed illumination of timescales and global pathways of vibrational energy transfer, (2) density functional theory and non-equilibrium molecular dynamics simulations, requiring leadership computing resources, which investigated vibrational energy transfer from the computational perspective, and (3) state-of-the-art methods for the deposition of high optical quality thin film samples of energetic materials, allowing detailed spectroscopic investigation. Although this report focused on describing our unpublished results, their connections to our published works, and some early conclusions, this experimental and computational work clearly reveals both conserved trends and distinct vibrational energy transfer dynamics in the three materials studied. The ongoing analysis, interpretation, and exploration of these ideas – to be detailed in future publications – will further demonstrate the considerable promise this collaborative approach holds in unraveling the fundamental chemical physics that govern the complex macroscopic properties of energetic materials.

These non-destructive means to investigate energy transfer dynamics, and thus shock sensitivity of energetic materials, has great promise for use as diagnostic tools for Sandia's programs. Extension of this work to study the dependence of vibrational energy transfer on morphology, chemical conformation (polymorphs) and chemical structure will enable the future application of this approach to more realistic energetic material systems. These more realistic systems can be bulk samples taken from fielded detonators or material taken from end-of-line production routes. Additionally, it is hard to overstate the scientific value in unraveling the mechanisms and timescales of energy transfer dynamics. Specific to the shock-to-detonation transition, this study probes one of the three leading initiation theories capable of explaining the ultrafast condensed phase chemistry that precedes detonation. As we move beyond heuristics or lump sum observations that guide our understanding of shock sensitivity, studies such as this will allow for precise design of energetic materials in the future where sensitivity is a design variable, rather than part of the end-product.

REFERENCES

1. Dlott, D. D.; Hambir, S.; Franken, J., The new wave in shock waves. ACS Publications: 1998.
2. Fried, L. E.; Manaa, M. R.; Pagoria, P. F.; Simpson, R. L., Design and synthesis of energetic materials. *Annual Review of Materials Research* **2001,** *31* (1), 291-321.
3. Dlott, D. D., New developments in the physical chemistry of shock compression. *Annual review of physical chemistry* **2011,** *62*, 575-597.
4. Powell, M. S.; Sakano, M. N.; Cawkwell, M. J.; Bowlan, P. R.; Brown, K. E.; Bolme, C. A.; Moore, D. S.; Son, S. F.; Strachan, A.; McGrane, S. D., Insight into the Chemistry of PETN Under Shock Compression Through Ultrafast Broadband Mid-Infrared Absorption Spectroscopy. *The Journal of Physical Chemistry A* **2020**.
5. Dlott, D. D.; Fayer, M. D., Shocked molecular solids: vibrational up pumping, defect hot spot formation, and the onset of chemistry. *The Journal of chemical physics* **1990,** *92* (6), 3798-3812.
6. Tokmakoff, A.; Fayer, M.; Dlott, D. D., Chemical reaction initiation and hot-spot formation in shocked energetic molecular materials. *The Journal of Physical Chemistry* **1993,** *97* (9), 1901-1913.
7. Chen, S.; Hong, X.; Hill, J. R.; Dlott, D. D., Ultrafast energy transfer in high explosives: Vibrational cooling. *The Journal of Physical Chemistry* **1995,** *99* (13), 4525-4530.
8. Chen, S.; Tolbert, W. A.; Dlott, D. D., Direct measurement of ultrafast multiphonon up-pumping in high explosives. *The Journal of Physical Chemistry* **1994,** *98* (32), 7759-7766.
9. Hong, X.; Chen, S.; Dlott, D. D., Ultrafast mode-specific intermolecular vibrational energy transfer to liquid nitromethane. *The Journal of Physical Chemistry* **1995,** *99* (22), 9102-9109.
10. Aubuchon, C.; Rector, K.; Holmes, W.; Fayer, M., Nitro group asymmetric stretching mode lifetimes of molecules used in energetic materials. *Chemical physics letters* **1999,** *299* (1), 84-90.
11. Berg, C.; Dlott, D. In *Picosecond dynamics of shock compressed and flash-heated nanometer thick films of δ-HMX*, Journal of Physics: Conference Series, IOP Publishing Ltd.: 2014; p 142004.
12. Shi, L.; Yu, P.; Zhao, J.; Wang, J., Ultrafast Intermolecular Vibrational Energy Transfer in Hexahydro-1, 3, 5-trinitro-1, 3, 5-triazine in Molecular Crystal by 2D IR Spectroscopy. *The Journal of Physical Chemistry C* **2020,** *124* (4), 2388-2398.
13. McGrane, S. D.; Barber, J.; Quenneville, J., Anharmonic vibrational properties of explosives from temperature-dependent Raman. *The Journal of Physical Chemistry A* **2005,** *109* (44), 9919-9927.
14. Ostrander, J. S.; Knepper, R.; Tappan, A. S.; Kay, J. J.; Zanni, M. T.; Farrow, D. A., Energy transfer between coherently delocalized states in thin films of the explosive pentaerythritol tetranitrate (PETN) revealed by two-dimensional infrared spectroscopy. *The Journal of Physical Chemistry B* **2017,** *121* (6), 1352-1361.
15. Yu, G.; Zeng, Y.; Guo, W.; Wu, H.; Zhu, G.; Zheng, Z.; Zheng, X.; Song, Y.; Yang, Y., Visualizing intramolecular vibrational redistribution in cyclotrimethylene trinitramine (RDX) crystals by multiplex coherent anti-Stokes Raman scattering. *The Journal of Physical Chemistry A* **2017,** *121* (13), 2565-2571.
16. Petersen, P. B.; Tokmakoff, A., Source for ultrafast continuum infrared and terahertz radiation. *Optics letters* **2010,** *35* (12), 1962-1964.
17. Mathieu, D., Sensitivity of energetic materials: Theoretical relationships to detonation performance and molecular structure. *Industrial & Engineering Chemistry Research* **2017,** *56* (29), 8191-8201.
18. Cole-Filipiak, N. C.; Knepper, R.; Wood, M.; Ramasesha, K., Sub-picosecond to Sub-nanosecond Vibrational Energy Transfer Dynamics in Pentaerythritol Tetranitrate. *The Journal of Physical Chemistry Letters* **2020,** *11*, 6664-6669.

19. Cole-Filipiak, N.; Marquez, M. P.; Knepper, R.; Harmon, R. A.; Wiese-Smith, D.; Schrader, P. E.; Wood, M.; Ramasesha, K. *Ultrafast Spectroscopic Studies of Vibrational Energy Transfer in Energetic Materials*; Sandia National Lab.(SNL-CA), Livermore, CA (United States); Sandia National …: 2019.
20. Ramasesha, K. Dynamics of water and aqueous protons studied using ultrafast multi-dimensional infrared spectroscopy. Massachusetts Institute of Technology, 2013.
21. Kresse, G., Ab initio molecular dynamics for liquid metals. *Journal of Non-Crystalline Solids* **1995,** *192*, 222-229.
22. Kresse, G.; Furthmüller, J., Efficiency of ab-initio total energy calculations for metals and semiconductors using a plane-wave basis set. *Computational materials science* **1996,** *6* (1), 15-50.
23. Mattsson, A. E.; Schultz, P. A.; Desjarlais, M. P.; Mattsson, T. R.; Leung, K., Designing meaningful density functional theory calculations in materials science—a primer. *Modelling and Simulation in Materials Science and Engineering* **2004,** *13* (1), R1.
24. Togo, A.; Chaput, L.; Tanaka, I., Distributions of phonon lifetimes in Brillouin zones. *Physical Review B* **2015,** *91* (9), 094306.
25. Togo, A.; Oba, F.; Tanaka, I., First-principles calculations of the ferroelastic transition between rutile-type and CaCl 2-type SiO 2 at high pressures. *Physical Review B* **2008,** *78* (13), 134106.
26. Togo, A.; Tanaka, I., First principles phonon calculations in materials science. *Scripta Materialia* **2015,** *108*, 1-5.
27. Baroni, S.; Resta, R., Ab initio calculation of the macroscopic dielectric constant in silicon. *Physical Review B* **1986,** *33* (10), 7017.
28. Gajdoš, M.; Hummer, K.; Kresse, G.; Furthmüller, J.; Bechstedt, F., Linear optical properties in the projector-augmented wave methodology. *Physical Review B* **2006,** *73* (4), 045112.
29. Pereverzev, A.; Sewell, T. D.; Thompson, D. L., Calculation of anharmonic couplings and THz linewidths in crystalline PETN. *The Journal of Chemical Physics* **2014,** *140* (10), 104508.
30. Bedrov, D.; Hooper, J. B.; Smith, G. D.; Sewell, T. D., Shock-induced transformations in crystalline RDX: A uniaxial constant-stress Hugoniostat molecular dynamics simulation study. *The Journal of chemical physics* **2009,** *131* (3), 034712.
31. Kroonblawd, M. P.; Sewell, T. D., Theoretical determination of anisotropic thermal conductivity for crystalline 1, 3, 5-triamino-2, 4, 6-trinitrobenzene (TATB). *The Journal of chemical physics* **2013,** *139* (7), 074503.
32. Plimpton, S., Fast parallel algorithms for short-range molecular dynamics. *Journal of computational physics* **1995,** *117* (1), 1-19.
33. Wood, M. A.; Strachan, A., Nonequilibrium reaction kinetics in molecular solids. *The Journal of Physical Chemistry C* **2016,** *120* (1), 542-552.
34. Wood, M. A.; Van Duin, A. C.; Strachan, A., Coupled thermal and electromagnetic induced decomposition in the molecular explosive αHMX; a reactive molecular dynamics study. *The Journal of Physical Chemistry A* **2014,** *118* (5), 885-895.
35. Martyna, G. J.; Tobias, D. J.; Klein, M. L., Constant pressure molecular dynamics algorithms. *The Journal of chemical physics* **1994,** *101* (5), 4177-4189.
36. Parrinello, M.; Rahman, A., Polymorphic transitions in single crystals: A new molecular dynamics method. *Journal of Applied physics* **1981,** *52* (12), 7182-7190.
37. Tuckerman, M. E.; Alejandre, J.; López-Rendón, R.; Jochim, A. L.; Martyna, G. J., A Liouville-operator derived measure-preserving integrator for molecular dynamics simulations in the isothermal–isobaric ensemble. *Journal of Physics A: Mathematical and General* **2006,** *39* (19), 5629.
38. Shinoda, W.; Shiga, M.; Mikami, M., Rapid estimation of elastic constants by molecular dynamics simulation under constant stress. *Physical Review B* **2004,** *69* (13), 134103.
39. Dullweber, A.; Leimkuhler, B.; McLachlan, R., Symplectic splitting methods for rigid body molecular dynamics. *The Journal of chemical physics* **1997,** *107* (15), 5840-5851.

40. Ceriotti, M.; Bussi, G.; Parrinello, M., Colored-noise thermostats à la carte. *Journal of Chemical Theory and Computation* **2010,** *6* (4), 1170-1180.
41. Ceriotti, M.; Bussi, G.; Parrinello, M., Langevin equation with colored noise for constant-temperature molecular dynamics simulations. *Physical review letters* **2009,** *102* (2), 020601.
42. Dettori, R.; Ceriotti, M.; Hunger, J.; Melis, C.; Colombo, L.; Donadio, D., Simulating Energy Relaxation in Pump–Probe Vibrational Spectroscopy of Hydrogen-Bonded Liquids. *Journal of chemical theory and computation* **2017,** *13* (3), 1284-1292.
43. Gruzdkov, Y. A.; Gupta, Y. M., Vibrational properties and structure of pentaerythritol tetranitrate. *The Journal of Physical Chemistry A* **2001,** *105* (25), 6197-6202.
44. Blöchl, P. E., Projector augmented-wave method. *Physical review B* **1994,** *50* (24), 17953.
45. Methfessel, M.; Paxton, A., High-precision sampling for Brillouin-zone integration in metals. *Physical Review B* **1989,** *40* (6), 3616.
46. Grimme, S.; Ehrlich, S.; Goerigk, L., Effect of the damping function in dispersion corrected density functional theory. *Journal of computational chemistry* **2011,** *32* (7), 1456-1465.
47. Perdew, J. P.; Burke, K.; Ernzerhof, M., Generalized gradient approximation made simple. *Physical review letters* **1996,** *77* (18), 3865.
48. Sorescu, D. C.; Rice, B. M.; Thompson, D. L., Theoretical studies of the hydrostatic compression of RDX, HMX, HNIW, and PETN crystals. *The Journal of Physical Chemistry B* **1999,** *103* (32), 6783-6790.
49. Müller-Plathe, F., A simple nonequilibrium molecular dynamics method for calculating the thermal conductivity. *The Journal of chemical physics* **1997,** *106* (14), 6082-6085.
50. Ciezak, J. A.; Jenkins, T. A.; Liu, Z.; Hemley, R. J., High-pressure vibrational spectroscopy of energetic materials: Hexahydro-1, 3, 5-trinitro-1, 3, 5-triazine. *The Journal of Physical Chemistry A* **2007,** *111* (1), 59-63.
51. Adams, B. M.; Bohnhoff, W. J.; Dalbey, K.; Eddy, J.; Eldred, M.; Gay, D.; Haskell, K.; Hough, P. D.; Swiler, L. P., DAKOTA, a multilevel parallel object-oriented framework for design optimization, parameter estimation, uncertainty quantification, and sensitivity analysis: version 5.0 user's manual. *Sandia National Laboratories, Tech. Rep. SAND2010-2183* **2009**.
52. Yan, B.-L.; Qin, H.; He, Z.-K.; Wei, Y.; Chang, K.; Guo, B.-L.; Tang, B.; Fan, D.-H.; Liu, Q.-J., Vibrational assignments and thermodynamic properties of triclinic TATB. *Physica B: Condensed Matter* **2018,** *546*, 1-9.

DISTRIBUTION

Email—Internal

Name	Org.	Sandia Email Address
Darcie Farrow	1528	dfarrow@sandia.gov
Kyran Mish	1555	kdmish@sandia.gov
Hongyou Fan	1815	hfan@sandia.gov
John Eberhart	2225	jaeberh@sandia.gov
Katherine Bogart	2225	khbogar@sandia.gov
Alexander Tappan	2554	astappa@sandia.gov
Leanna Minier	2554	lminier@sandia.gov
Sean Maharrey	2554	spmahar@sandia.gov
Daniel Bufford	2555	dcbuffo@sandia.gov
Jennifer Dellinger	2555	jdellin@sandia.gov
Kathy Alam	2555	mkalam@sandia.gov
David Chandler	8000	chand@sandia.gov
LeRoy Whinnery	8200	llwhinn@sandia.gov
Jeffrey Kay	8248	jjkay@sandia.gov
Sarah Allendorf	8300	swallen@sandia.gov
Dawn Skala	8344	dmsabel@sandia.gov
Craig Taatjes	8350	cataatj@sandia.gov
David Osborn	8353	dlosbor@sandia.gov
Nathalie Le Galloudec	8484	nlegall@sandia.gov
Kenneth C. Chen	9411	kcchen@sandia.gov
Tracie Durbin	9411	tldurbi@sandia.gov
Technical Library	01977	sanddocs@sandia.gov

Email—External

Name	Company Email Address	Company Name
Michael Armstrong	armstrong30@llnl.gov	Lawrence Livermore National Lab
Matt Kroonblawd	kroonblawd1@llnl.gov	Lawrence Livermore National Lab
Leanna Minier		Air Force Research Lab
Shawn McGrane	mcgrane@lanl.gov	Los Alamos National Lab
Laura Smilowitz	smilo@lanl.gov	Los Alamos National Lab

This page left blank

Sandia National Laboratories

Sandia National Laboratories is a multimission laboratory managed and operated by National Technology & Engineering Solutions of Sandia LLC, a wholly owned subsidiary of Honeywell International Inc. for the U.S. Department of Energy's National Nuclear Security Administration under contract DE-NA0003525.